ANALYSIS OF MECHANO-ELECTROCHEMICAL COUPLING IN INTERCALATION ELECTRODES

A Thesis

by

NIHAR KAMLESH KOTAK

Submitted to the Office of Graduate and Professional Studies of
Texas A&M University
in partial fulfillment of the requirements for the degree of

MASTER OF SCIENCE

Chair of Committee,	Partha P. Mukherjee
Committee Members,	Debjyoti Banerjee
	Sarbajit Banerjee
Head of Department,	Andreas A. Polycarpou

May 2016

Major Subject: Mechanical Engineering

ABSTRACT

Lithium ion batteries (LIB), owing to their high energy and power density, have gained popularity in portable electronics and automotive markets. Diffusion induced stress (DIS), due to intercalation of lithium during lithiation/delithiation process is one of the main causes of mechanical degradation in LIB. The microcracks formed hinder the diffusion of lithium inside the active particle. Also, the microcracks linked to the surface of the particle are exposed to the electrolyte and are electrochemically active.

This study investigates the mechano-electrochemical coupling observed in intercalation electrodes. The interdependence between microcrack formation and lithium concentration distribution in the active particle and its effect on the performance of LIB has been analyzed. A microcrack prediction model has been developed that estimates microcrack formation at each time step based on the DIS calculated using the concentration gradients evaluated from the concentration profile. The microcracks affect the transport of lithium within the particle in two opposing ways. On one hand, microcracks decrease the local diffusivity of the active material thereby hindering lithium diffusion. On the other hand, microcracks emanating from the surface of the particle are electrochemically active and enhance lithium diffusion by allowing electrochemical reactions inside the active particle at the microcrack-electrolyte interface, thereby reducing the effective diffusion length. Thus, microcrack formation leads to a change in the electrochemically active surface area of the electrode. Lithium source/sink terms are

introduced along the electrochemically active microcracks to simulate the electrochemical reactions. The non-uniform microcrack patterns predicted by the mechano-electrochemically coupled model closely resemble the patterns observed in SEM images of LIB electrodes.

The performance curve obtained can help identify the effect of mechanical degradation on the performance of the battery and thereby provide a guideline for optimizing the physicochemical factors to leverage mechanical degradation for better cell performance.

This thesis is dedicated to my parents and grand parents

ACKNOWLEDGEMENTS

I would like to thank my thesis adviser and mentor, Dr. Partha P. Mukherjee (Mechanical Engineering, TAMU), for his continuous encouragement as well as technical and financial support during this academic journey. I would also like to thank my committee members, Dr. Sarbajit Banerjee (Chemical Engineering, TAMU) and Dr. Debjyoti Banerjee (Mechanical Engineering, TAMU) for their valuable guidance and support.

Special thanks to my colleagues at ETSL for their kind cooperation and support during the span of my research. Thanks also go to my friends, colleagues and the department faculty and staff for making my time at Texas A&M University a great experience.

Finally, I would like to thank my mother, father and grandparents for their continuous encouragement and support.

TABLE OF CONTENTS

Page

ABSTRACT ii

ACKNOWLEDGEMENTS v

TABLE OF CONTENTS vi

LIST OF FIGURES vii

CHAPTER I INTRODUCTION AND LITERATURE REVIEW 1

Introduction 1
Literature review 6

CHAPTER II COMPUTATIONAL METHODOLOGY 10

Transport model 10
Mechanics model 14
Mapping between the transport and mechanics meshes 17
Reduction in diffusivity 18
Classification of nodes in the transport mesh 19
Formulating the increase of electrochemical electrode area with time 21
Determining the magnitude of electrochemical reaction terms 23

CHAPTER III SINGLE DISCHARGE 27

Effect of discharge rate 44
Effect of particle size 47
Effect of temperature 50

CHAPTER IV CYCLING BEHAVIOR 57

Effect of rate of operation 66
Effect of temperature 71

CHAPTER V CONCLUSION AND FUTURE SCOPE 78

REFERENCES 80

LIST OF FIGURES

Page

Figure 1: Schematic diagram of a LIB 3

Figure 2: Transgranular crack in graphite 7

Figure 3: Possible transport control volumes 12

Figure 4: Schematic representation of Lattice Spring Model 15

Figure 5: Mapping between the mechanics and transport meshes 18

Figure 6: Negative effect of microcrack on lithium transport 19

Figure 7: Classification of nodes in the active particle 20

Figure 8: Model flowchart 25

Figure 9: Evolution of fracture density (%) 29

Figure 10: Distribution of electrochemically active (red colored) and inactive microcracks (black colored) at (a)120 sec (b) 600 sec (c) 1080 sec (d) 1320 sec – end of discharge 32

Figure 11: Evolution of effective, ineffective and total electrochemical area of the electrode 33

Figure 12: Concentration contour plot with superimposed microcracks at (a)120 sec (b) 600 sec (c) 1080 sec (d) 1320 sec – end of discharge 35

Figure 13: Concentration contour plots showing only the effective electrochemical area at (a) 1080 sec (b) 1320 sec – end of discharge 36

Figure 14: Model comparison – fracture density (%) evolution 37

Figure 15: Model comparison - concentration contour plots with microcracks superimposed at the end of discharge (a) with mechanics (b) with mechanics + reactions in cracks 39

Figure 16: Model comparison - radial distribution of fracture density (%) at the end of discharge 39

Figure 17: Model comparison - angular distribution of average lithium concentration and fracture density at the end of discharge (a) with mechanics (b) with mechanics + reactions in cracks 41

Figure 18: Model comparison - electrochemical area evolution 41

Figure 19: Model comparison - performance 43

Figure 20: Effect of rate of discharge – fracture density 45

Figure 21: Effect of rate of discharge – electrochemical Area 46

Figure 22: Effect of rate of discharge – performance 46

Figure 23: Effect of particle size – fracture density 48

Figure 24: Effect of particle size – electrochemical area 49

Figure 25: Effect of particle size – performance 50

Figure 26: Effect of temperature – normalized diffusivity (D/D_0) 51

Figure 27: Effect of temperature – fracture density 52

Figure 28: Effect of temperature – electrochemical area 53

Figure 29: Effect of temperature – performance 54

Figure 30: Mechanical degradation phase map for (a) 0°C (b) 25°C and (c) 50°C 56

Figure 31: Concentration contour plots for cycling simulations 59

Figure 32: Concentration contour plots for cycling simulations (cont.) 60

Figure 33: Concentration contour plots with microcracks superimposed (a) end of 1st discharge (b) end of 2nd discharge (c) end of 3rd discharge (d) end of 4th discharge 61

Figure 34: Cycling behavior - fracture density 62

Figure 35: Cycling behavior - electrochemical area 62

Figure 36: Cycling behavior – normalized concentration 63

Figure 37: Cycling behavior – performance 64

Figure 38: Cycling behavior – cycle wise performance 64

Figure 39: Cycling behavior – capacity fade.....65

Figure 40: Effect of rate of operation – fracture density (a) 2C (b) 1C (c) C/2 67

Figure 41: Concentration contour plots at the end of 10^{th} discharge cycle (a) 2C (b) 1C (c) C/2 67

Figure 42: Effect of rate of operation – electrochemical area (a) 2C (b) 1C (c) C/2 68

Figure 43: Effect of rate of operation – normalized concentration (a) 2C (b) 1C (c) C/2.....69

Figure 44: Effect of rate of operation – performance (a) 2C (b) 1C (c) C/2.....70

Figure 45: Cycling behavior – cycle wise performance.....71

Figure 46:Effect of temperature – fracture density (a) 0°C (b) 25°C (c) 50°C.....72

Figure 47: Concentration contour plots at the end of 10^{th} discharge cycle (a) 0°C (b) 25°C (c) 50°C 73

Figure 48: Effect of temperature – electrochemical area (a) 0°C (b) 25°C (c) 50°C.....74

Figure 49: Effect of temperature – normalized concentration (a) 0°C (b) 25°C (c) 50°C 75

Figure 50: Effect of temperature – performance (a) 0°C (b) 25°C (c) 50°C.....76

Figure 51: Effect of temperature – cycle wise performance 77

CHAPTER I

INTRODUCTION AND LITERATURE REVIEW

Introduction

Excessive dependence on fossil fuels to match the increasing energy demands of the industrially and technologically advancing world can have grave consequences for the future generations. The present energy generation, supply and distribution practices are exerting severe pressure on the environment and hence cannot be continued indefinitely [1-4]. Switching to renewable sources of energy is the most logical alternative in trying to restore and maintain the environmental balance [5-8]. However, keeping in mind the intermittent nature of the renewable energy sources, it is important to be able to efficiently store the energy from these sources to guarantee reliability and make renewable sources a viable option [9-12]. Hence, in the past decade, a lot of emphasis has been placed on investigating and commercializing different battery chemistries. Lithium ion battery (LIB) is a result of such research efforts. Owing to its high energy and power density, LIB have emerged as a probable solution to the energy storage problems [13, 14]. Due to excessive consumption of fossil fuels in transportation systems, electrification of automotive drive trains marks the first step towards reducing the fossil fuel dependence [15-19]. Over the last decade, development of LIB has imparted great impetus to vehicle electrification [20-22].

Figure 1 describes in brief, the working of a lithium ion battery. LIB, typically comprises of three main components, namely cathode material, anode material and a porous separator. The cathode material, which is usually a combination of $LiCoO_2$, $LiNiO_2$ and $LiMnO_2$, is in contact with the cathode current collector made of aluminum (Al) foil [23, 24]. A layer of porous polymer flooded with electrolyte separates the cathode material from the anode material. Graphite is the most widely used anode material for LIB [25, 26]. Generally, the anode current collector is made of copper (Cu). During the discharge process, lithium ions move from the anode to the cathode via the electrolyte while the electrons move in the same direction through the external circuit via the current collectors. This motion of electrons constitutes the electric current and delivers energy to the devices connected in the external circuit. During the charge process, the direction of motion of lithium and electrons reverses. This requires power to be supplied to the cell from outside sources.

Recent years have witnessed an enormous boost in the popularity of LIB. Developments in LIB have imparted great impetus to vehicle electrification. Owing to its low weight, high capacity and good performance, LIB have become a preferred power source for numerous other portable consumer applications as well [24, 27-29]. Despite these promising features, the service life of LIB systems is considerably limited by the degradation of active electrode material upon repeated charge-discharge cycles [30-32].

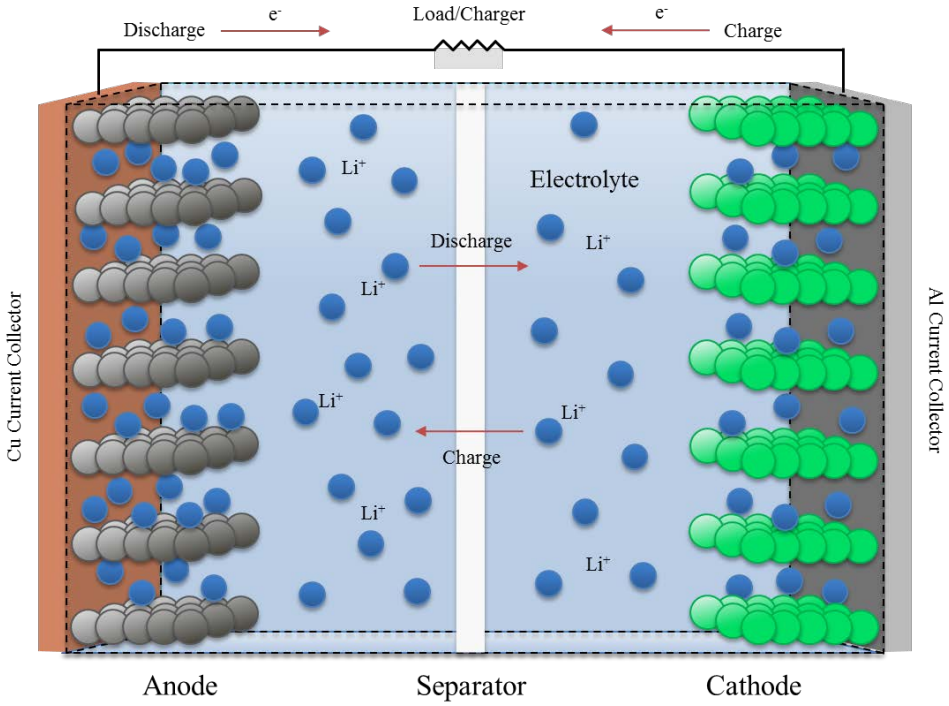

Figure 1: Schematic diagram of a LIB

Mechanical degradation in LIB electrodes is identified as one of the key factors limiting the life and performance of LIB [33-35]. Intercalation/de-intercalation of lithium in the active lattice sites can lead to changes in the specific volume of the active particle. These volume changes give rise to mechanical strains within the lattice of the active particle [36-38]. Diffusion induced stress (DIS) is a result of such mechanical strains. If the DIS exceeds the fracture strength, microcracks are formed[39]. Formation of new microcracks and fast propagation of existing defects in the active particle are the main modes of mechanical degradation [34, 40]. The microcracks can affect the cell performance in two opposing ways:

1. **Positive effect:** Microcracks spanning from the surface of the particle are exposed to electrolyte and are electrochemically active thereby reducing the diffusion length and facilitating the transport of lithium; improving cell performance.

2. **Negative effect:** Microcracks disconnected from the surface of the particle are electrochemically inactive and obstruct lithium diffusion; deteriorating cell performance.

Upon repeated charge-discharge cycles, there also exists a possibility of the active particle breaking off into smaller particles some of which may get isolated due to poor contact with conductive additives. Thus, disintegration of the active particle can lead to irreversible loss of capacity [41, 42]. Further, mechanical degradation also intensifies the extent of chemical degradation by providing a greater active material-electrolyte interface area for the formation of Solid Electrolyte Interphase (SEI). The SEI formation and growth over the increased interface area directly results in the loss of cyclable lithium ions and hence, capacity [43-49].

Improving the life-span of lithium-ion battery systems has been the key research emphasis lately. In that direction, fundamental understanding of the mechanisms underlying the degradation phenomena observed in the battery electrodes is of prime importance [50]. Several studies to understand the deteriorating effects of mechanical degradation mechanisms have been carried out over the last few decades. But, to the best of author's knowledge, none of the studies investigate the positive effect of microcrack formation and propagation wherein the surface microcracks facilitate diffusion of lithium. For a more realistic prediction of the effect of mechanical degradation on cell

performance, it is necessary to include both, the facilitating as well as the hindering effect of microcracks on lithium transport.

The primary objective of this study is to develop a mathematical model that predicts the effect of mechanical degradation on the cell performance. In doing so, it should incorporate both, the positive (aiding lithium diffusion) as well as the negative (hindering lithium diffusion) effects of mechanical degradation. As a secondary objective, phase maps for mechanical degradation and performance will be developed to act as a guideline for selecting the optimal set of physicochemical factors to enhance cell performance.

Literature review

Recent years have seen an unprecedented research emphasis on improving the performance, life cycle and safety associated with LIB. Many efforts have been made to study mechanical degradation - one of the major degradation mechanisms for LIB electrodes. Pioneering work in the direction of quantifying the mechanical stress generated in the active particle during intercalation was conducted by Christensen and Newman [51, 52]. This model was later applied to lithium-manganese-oxide cathode materials. It was observed that smaller particle size and larger aspect ratio reduces the DIS in the particle resulting in better performance [38]. Wang *et. al* conducted experiments with $LiCoO_2$ – Li cells to study the microcrack formation and propagation in $LiCoO_2$ cathodes using transmission electron microscopy (TEM) [53]. The TEM images of $LiCoO_2$ particles from cycled cathode indicated severe mechanical damage by formation of large microcracks. Similarly, presence of transgranular cracks in graphite active particles was pointed out by the SEM images of graphite electrode taken by Harris *et. al*. [54, 55] (see fig. 2). An electrochemical shock map based on linear elastic fracture mechanics (LEFM) failure criterion was developed by Woodford *et. al*. It helped predicting the onset of failure based on the C rate, particle size and the fracture toughness of the active material [56]. Location and orientation dependent progressive propagation of preexisting defects in cylindrical graphite electrode particles was also studied [57]. A dimensionless number, equivalent to Biot number in heat-transfer, was proposed by Cheng and Verbrugge. They showed that the intercalate concentration and hence, the microcrack initiation is solely governed by

this dimensionless number [58]. The fracture of electrodes of LIBs operated at high currents was investigated by Zhao *et.al* [59].

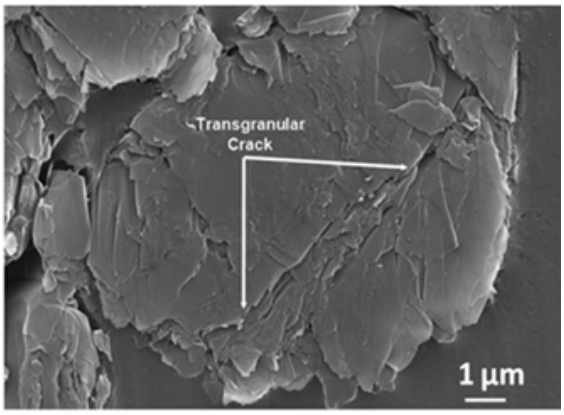

Figure 2: Transgranular crack in graphite [54]

A stochastic model to investigate the impact of fracture on lithium ion diffusion by introducing a damage parameter was proposed by Barai *et. al*. The model developed by them used the random lattice spring formalism coupled with solid-state diffusion of lithium in active particles. They also proposed a fracture phase map that can serve as a guideline for selecting the operating and design parameters to abate fracture formation [60].

To the best of author's knowledge, most of the computational models developed to study mechanical degradation so far neglect the electrochemical reactions taking place in the newly formed microcracks which are linked to the surface of the particle. But as the SEM images of graphite and TEM images of $LiCoO_2$ show, the microcracks give rise to

large new surface areas which if exposed to the electrolyte can significantly contribute to the lithium generating/consuming electrochemical reactions. Desphande *et. al* developed a model that simulates the loss of capacity owing to the formation and growth of SEI layer over the microcrack surface [36]. Xu *et. al* adopted the model developed by Despande *et. al* and investigated the loss of capacity due to crack propagation on the negative electrode [61]. While both the models mentioned above rudimentarily account for the increase in the solid particle – electrolyte interfacial area, they do not account for the electrochemical reactions at the microcrack surfaces that contribute to the lithium flux acting on the particle.

This work is an extension of the fracture model developed by Barai *et. al*[60]. A mathematical model that can mimic the two-way coupling between the mechanical and electrochemical phenomena has been developed and is clubbed with the fracture model. Apart from the hindrance caused to lithium transport, the electrochemical reactions taking place at the microcrack-electrolyte interface are also taken into account. The resultant electrochemically induced mechanical degradation in the active particle and its effect on the electrochemical reactions for subsequent time instances has been studied. The effect of mechanical degradation on the performance of the LIB is also investigated. Mechanical degradation and performance phase maps have been developed that help in predicting the mechanical damage endured by the electrode and the performance expected from the cell for a given set of operating and battery parameters. This can help in the development of new materials for LIB with enhanced mechanical properties and also serve as a guideline for leveraging mechanical degradation to enhance the LIB performance.

The model developed in this study is elaborately discussed in the subsequent chapters. To begin with, the methodology behind the model is described in detail in the next chapter. Chapter III and IV are dedicated to analyzing the simulation results. Chapter III specifically deals with thorough investigation of the mechanical degradation taking place in the anode particle during the first discharge. In chapter IV, mechanical degradation of the electrodes due to cell cycling is studied. In both of these chapters, the key factors that influence the mechanical degradation and performance of LIB are identified. Several test cases are then discussed to elucidate the effect of these influencing factors on mechanical degradation and cell performance.

CHAPTER II

COMPUTATIONAL METHODOLOGY

Transport model

Following the assumptions justified by the Single Particle Model, each electrode has been assumed to consist of uniformly sized spherical intercalation particles [62-65]. Ionic conductivity of the electrolyte has been assumed to be very high, resulting in negligible lithium ion concentration gradient in the electrolyte phase. Hence, constant galvanostatic current, from all directions, acts upon the active particle.

Electrochemical reactions take place at the active particle – electrolyte interface. The rate of electrochemical reactions depend on the rate at which current is drawn from the battery (C-rate). During the discharge process, lithium from the anode active particle is consumed by the electrochemical reactions and is transported, via the electrolyte, to the cathode active particle where it is generated back. During the charge process, the direction of lithium transport is opposite. Lithium generated/consumed by the electrochemical reactions must diffuse through the active particle. As the ionic conductivity of the electrolyte is assumed to be very high, diffusion of lithium inside the active particle will limit the capacity of the cell. Diffusion of lithium within the active particle is governed by Fick's laws of diffusion [63, 66, 67].

Hence, the Li ion concentration in the active particle has been calculated using the following equation:

$$\frac{\delta c\left(\vec{x},t\right)}{\delta t}=\vec{\nabla}\bullet\left(\underset{\sim}{D}\left(\vec{x},t\right)\bullet\vec{\nabla}c\left(\vec{x},t\right)\right) \tag{2.1}$$

Depending on the process (charge/discharge) being simulated, the initial concentration of lithium inside the active particle is fixed.

$$c_i\left(x,0\right)=c_{ini} \tag{2.2}$$

Constant lithium mass flux $\left(J=\frac{I}{F\cdot S_i}\right)$ as a result of the constant galvanostatic current$\left(I\right)$ from all directions provides one boundary condition. The other boundary condition is obtained by noting the symmetry of the problem that results in zero mass flux of lithium at the center.

$$\left(D_i\frac{\delta c_i}{\delta r}\right)\Bigg|_{r=0}=0 \tag{2.3}$$

$$\left(D_i\frac{\delta c_i}{\delta r}\right)\Bigg|_{r=R}=-J \tag{2.4}$$

Initially, only the surface of the particle is electrochemically active and hence, responsible for lithium mass flux. But when coupled with a mechanics model for the electrode, microcracks emanating from the surface penetrate into the particle forming new

active particle-electrolyte interface. The electrochemical reactions taking place at these interfacial regions start contributing significantly to the lithium mass flux. This lithium mass flux has been captured in our model by introducing lithium source/sink terms in the concentration equations at the respective mechanically damaged concentration control volumes.

Figure 3 illustrates the three possible types of control volumes that exist within the active particle.

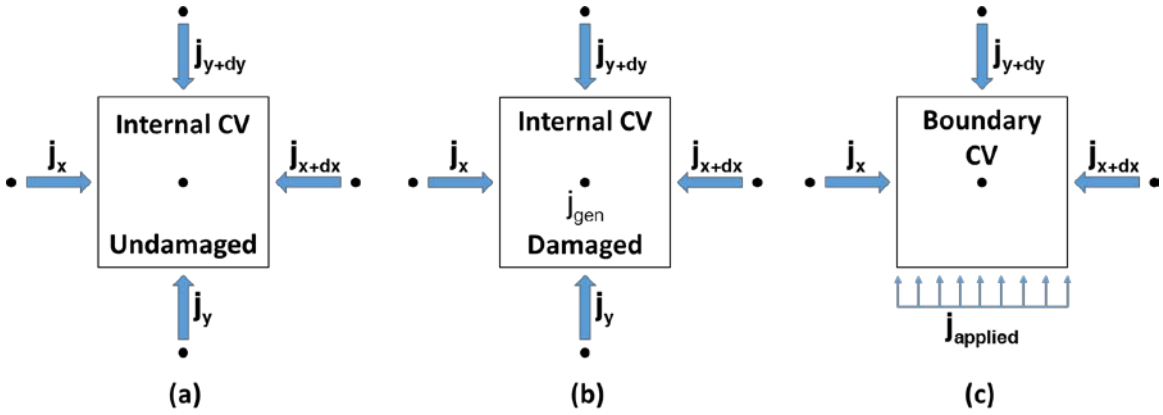

Figure 3: Possible transport control volumes

The general discretized equation for a control volume can be written as:

$$D_e \times A_y \left(\frac{c_{i+1,j} - c_{i,j}}{\Delta x} \right) + D_w \times A_y \left(\frac{c_{i-1,j} - c_{i,j}}{\Delta x} \right) + D_n \times A_x \left(\frac{c_{i,j+1} - c_{i,j}}{\Delta y} \right) + \ldots$$
$$\ldots + D_s \times A_x \left(\frac{c_{i,j-1} - c_{i,j}}{\Delta y} \right) + j_{applied} \times A_{surf} + j_{gen} \times V_{cv} = V_{cv} \times \left(\frac{c_{i,j} - c_{i,j}^{t-1}}{\Delta t} \right) \quad (2.5)$$

Depending upon the type of control volume, the above equation can be further simplified. For an undamaged boundary control volume, the generation term will be zero.

$$D_e \times A_y \left(\frac{c_{i+1,j} - c_{i,j}}{\Delta x} \right) + D_w \times A_y \left(\frac{c_{i-1,j} - c_{i,j}}{\Delta x} \right) + D_n \times A_x \left(\frac{c_{i,j+1} - c_{i,j}}{\Delta y} \right) \ldots$$
$$\ldots + D_s \times A_x \left(\frac{c_{i,j-1} - c_{i,j}}{\Delta y} \right) + j_{applied} \times A_{surf} = V_{cv} \left(\frac{c_{i,j} - c_{i,j}^{t-1}}{\Delta t} \right) \quad (2.6)$$

For an internal control volume having a microcrack passing through it, the flux terms will be zero while the generation term will have a finite value.

$$D_e \times A_y \left(\frac{c_{i+1,j} - c_{i,j}}{\Delta x} \right) A_y + D_w \times A_y \left(\frac{c_{i-1,j} - c_{i,j}}{\Delta x} \right) + D_n \times A_x \left(\frac{c_{i,j+1} - c_{i,j}}{\Delta y} \right) \ldots$$
$$\ldots + D_s A_x \left(\frac{c_{i,j-1} - c_{i,j}}{\Delta y} \right) + j_{gen} \times V_{cv} = V_{cv} \left(\frac{c_{i,j} - c_{i,j}^{t-1}}{\Delta t} \right) \quad (2.7)$$

For an internal control volume without any microcracks, both the flux and generation terms will be zero.

$$D_e \times A_y \left(\frac{c_{i+1,j} - c_{i,j}}{\Delta x} \right) + D_w \times A_y \left(\frac{c_{i-1,j} - c_{i,j}}{\Delta x} \right) \ldots$$
$$\ldots + D_n \times A_x \left(\frac{c_{i,j+1} - c_{i,j}}{\Delta y} \right) + D_s \times A_x \left(\frac{c_{i,j-1} - c_{i,j}}{\Delta y} \right) = V_{cv} \left(\frac{c_{i,j} - c_{i,j}^{t-1}}{\Delta t} \right) \quad (2.8)$$

Above equations satisfy the conservation of mass locally, thereby guaranteeing global mass balance.

Mechanics model

In order to capture the mechanical degradation in the battery electrodes, Barai and Mukherjee developed a stochastic methodology that is based on random lattice spring model [60, 68, 69]. In the current study, we adopt this mechanical model and couple it with the transport model described above. The model considers the active particle as a grid of lumped point masses, each connected to its immediate neighbors by springs. To account for Poisson's ratio, the springs are assumed to have two stiffness constants, one along the axial (k_n) and shear direction (k_s) each. The Poisson's ratio is then given by:

$$\nu = \frac{k_n - k_s}{3k_n + k_s} \quad (2.9)$$

Each lumped mass at the node is connected to six neighbors forming a triangular grid as shown in fig. 4.

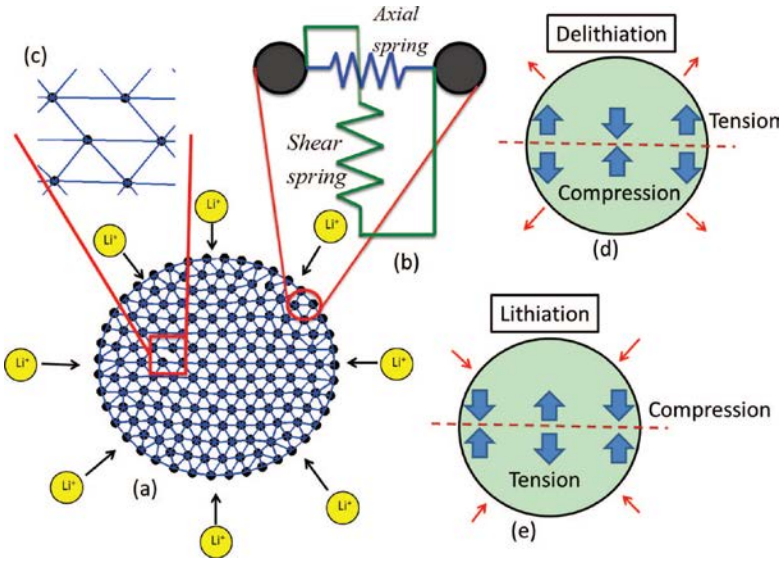

Figure 4: Schematic representation of Lattice Spring Model[60]

Each spring follows the Hooke's law and hence, the local force in the spring can be related to its displacement as follows:

$$\bar{f} = \kappa \bar{u} \tag{2.10}$$

$$\begin{bmatrix} f_{x1} \\ f_{x2} \\ f_{x3} \\ f_{x4} \end{bmatrix} = \begin{bmatrix} k_n & 0 & -k_n & 0 \\ 0 & k_s & 0 & -k_s \\ -k_n & 0 & k_n & 0 \\ 0 & -k_s & 0 & k_s \end{bmatrix} \begin{bmatrix} u_{x1} \\ u_{x2} \\ u_{x3} \\ u_{x4} \end{bmatrix} \tag{2.11}$$

where $\bar{f}$ represents the local force vector, κ represents the local stiffness matrix and $\bar{u}$ represents the local displacement vector. The local stiffness matrices are then assembled

using transformation matrix to form the global stiffness matrix. The axial displacement in the springs as a result of lithium diffusion is then given by,

$$\Delta u = \omega \times \Delta c \times l \tag{2.12}$$

Here, Δu represents the diffusion induced displacement, ω represents the diffusion expansion coefficient for graphite, Δc is the incremental change in lithium concentration and l is the length of the spring element. The local force vectors are then assembled to form a global force matrix $(\vec{F})$. The equilibrium force distribution is then calculated by solving the quasistatic force equilibrium equation 2.13,

$$\frac{\delta \vec{\sigma}}{\delta \vec{x}} + \vec{B} = \rho \vec{u} = 0 \tag{2.13}$$

where $\vec{\sigma}$ is the stress tensor and $\vec{B}$ is the body force vector (which is zero for the problem at hand)

The strain energy for each spring can then be calculated from the quasistatic equilibrium force and displacement distributions using:

$$E = \frac{1}{2} \vec{F} \times \vec{u} \tag{2.14}$$

The range of threshold energy for the springs is decided based on theory of elasticity considerations. The threshold energy for the springs is then randomly distributed

within that range. If the strain energy for a spring exceeds the threshold value, the spring is considered to be irreversibly broken.

$$E > E_t \text{ , Failure criteria} \quad (2.15)$$

Mapping between the transport and mechanics meshes

In order to simulate the coupling between mechanical degradation and electrochemical behavior of the active particles, it is important to locate the control volumes in the transport mesh that correspond to the broken spring elements in the mechanics mesh. For this purpose, a mapping function has been developed.

For example, consider the schematic diagram shown in fig. 5. To the left, is shown the active particle with a single microcrack propagating from the surface. Each segment in the coarse triangular grid represents a spring element. The red segments, in particular, represent the spring elements that are broken. As the spring elements break, they provide a path for the electrolyte (represented by grey color) to enter into the particle. This electrolyte path is mapped into the transport mesh, represented by blue color, in the inset figure - detail A. For this purpose, the coordinates of the center of the broken springs are calculated. These points are mapped to four nodal points having their x & y coordinates as the floor-ceiling combinations of the parent point. The bold blue nodes in detail A are the transport mesh images of the microcracks. The control volumes for these nodes will have electrochemical reaction terms included in lithium concentration calculations.

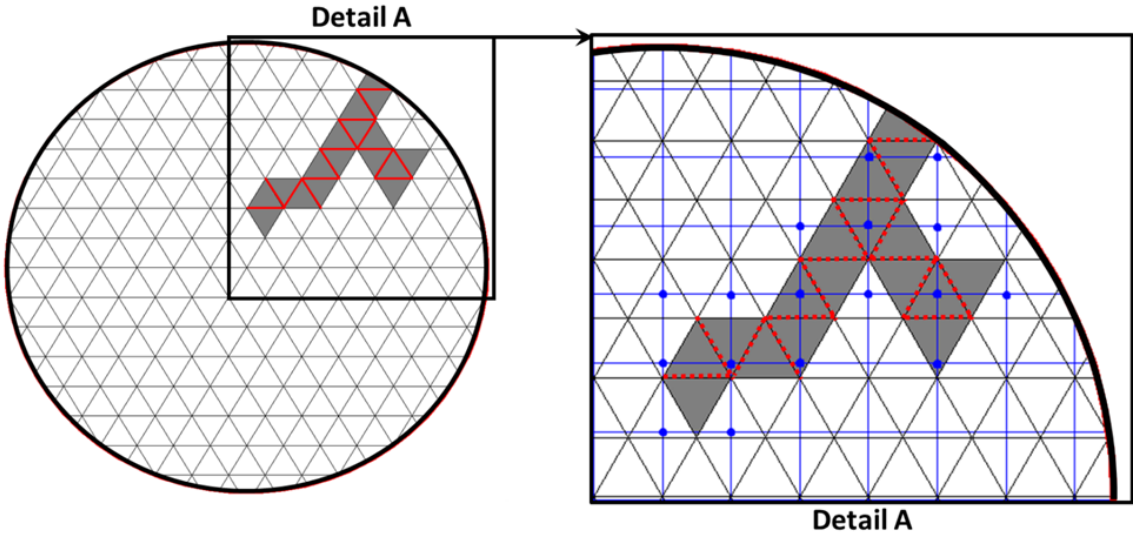

Figure 5: Mapping between the mechanics and transport meshes

Reduction in diffusivity

The microcracks formed, hinder the diffusion of lithium as the lithium atoms now have to take a tortuous path around the microcracks. This obstruction to lithium transport caused by the microcracks was accounted by Barai & Mukherjee, by introducing a damage parameter - crack effect (α) (see fig. 6). Crack effect is the fraction by which a microcrack reduces the diffusivity of the active material in its vicinity. Thus, crack effect can vary from 0 to 1. Crack effect value 1 corresponds to microcracks having no reduction in the diffusivity.

$$D_{effective} = \alpha D_{original} \tag{2.16}$$

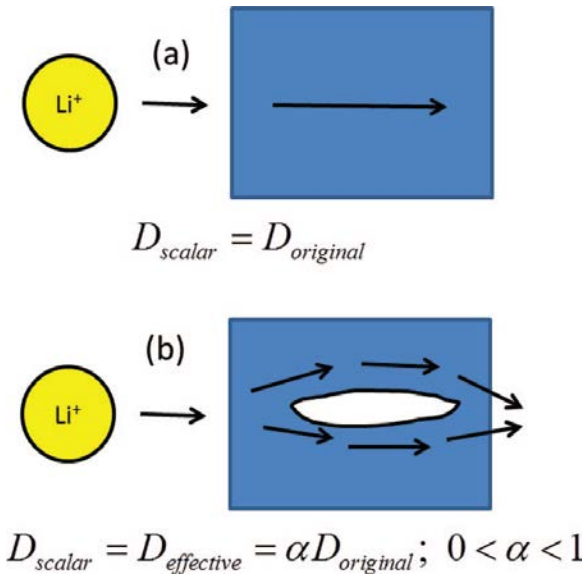

Figure 6: Negative effect of microcrack on lithium transport [60]

Classification of nodes in the transport mesh

Let N_{surf} be the total number of nodes that lie on the particle boundary and let $N_{vol,fracture}$ be the number of number of internal nodes with microcracks passing through the control volume. Now, the boundary nodes further, may or may not have a microcrack passing through their control volumes. Let $N_{surf,fracture}$ denote the number of boundary control volumes with microcracks and $N_{surf,intact}$ denote the number of boundary control volumes that do not have microcracks. Therefore,

$$N_{surf} = N_{surf,fracture} + N_{surf,intact} \tag{2.17}$$

Note that N_{surf} is constant throughout the simulation while $N_{surf,fracture}$ and $N_{surf,intact}$ dynamically change with time. Fig. 7 illustrates this hierarchical classification.

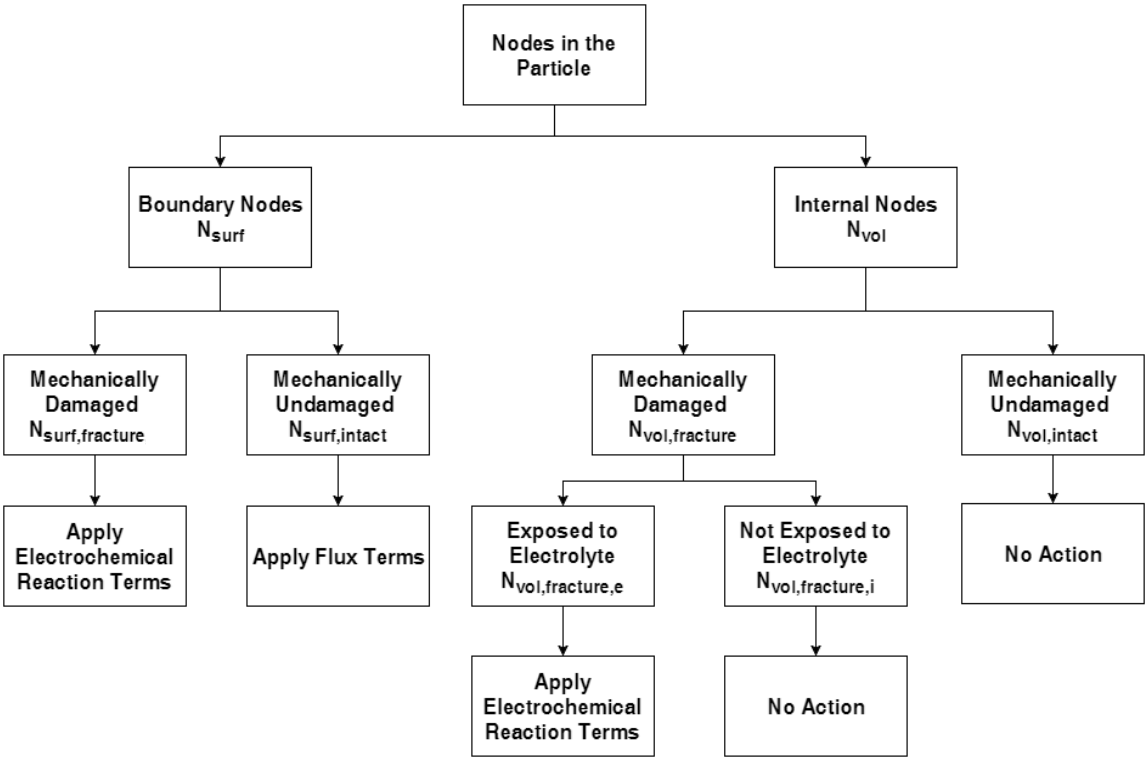

Figure 7: Classification of nodes in the active particle

Formulating the increase of electrochemical electrode area with time

Initially (t=0), only the surface area of the particle is electrochemically active. The surface area of the particle can be considered to be proportional to the number of control volumes that lie on the boundary of the particle. Hence,

$$A_e(0) = A_{surf,particle} \propto N_{surf} \tag{2.18}$$

After time t (t>0), microcracks start propagating in the particle. Now, along with the surface area of the particle, the microcrack-electrolyte interface also contributes to the electrochemically active area. Thus, the electrochemical area can now be considered to be proportional to the sum of control volumes that lie on the boundary of the particle and the control volumes with electrochemically active microcracks. Hence,

$$A_e(t) = A_{surf,particle} + A_{microcrack} \propto N_{surf} + N_{vol,fracture,e} \tag{2.19}$$

Applying unitary method gives,

$$\frac{A_e(t)}{A_e(0)} = \frac{A_e(t)}{A_{surf,particle}} = \left(\frac{N_{surf} + N_{vol,fracture,e}}{N_{surf}} \right) \tag{2.20}$$

This gives us a relation between the electrochemical area at time t and the surface area of the particle.

$$A_e(t) = A_{surf,particle} \left(\frac{N_{surf} + N_{vol,fracture,e}}{N_{surf}} \right) \tag{2.21}$$

Hence, knowing the surface area of the particle, the electrochemical area at any time t can be calculated using the equation (2.21).

For a constant current discharge, lithium mass flux, that is constant in all directions, must scale inversely with respect to the electrochemical area. As the electrochemical area increases, lithium mass flux must decrease to maintain constant current.

$$J_{applied}(t) \times A_e(t) = J_{applied}(0) \times A_e(0) \tag{2.22}$$

Hence, dynamic value of lithium flux can be calculated using the following equation.

$$J_{applied}(t) = J_{applied}(0) \times \left(\frac{N_{surf}}{N_{surf} + N_{vol,fracture,e}} \right) \tag{2.23}$$

Thus, constant current is maintained.

Determining the magnitude of electrochemical reaction terms

The magnitude of electrochemical reaction terms is determined maintaining the mass balance. Total lithium that enters the particle per second at time t can be given by equation (2.24), where the total electrochemical area at time t ($A_e(t)$), is split into its components:

- electrochemical area due to boundary control volumes that are intact $\left(\propto N_{surf,intact}(t)\right)$
- electrochemical area due to boundary control volumes that are mechanically damaged $\left(\propto N_{surf,fracture}(t)\right)$
- electrochemical area due to internal control volumes that are mechanically damaged and electrochemically active $\left(\propto N_{vol,fracture,e}(t)\right)$

$$\begin{aligned}\dot{m}_{Li} &= J_{applied}(t) \times A_e(t) \\ &\propto J_{applied}(t) \times \left(N_{surf,intact}(t) + N_{surf,fracture}(t) + N_{vol,fracture,e}(t)\right)\end{aligned} \tag{2.24}$$

$$\begin{aligned}\therefore m_{Li} \propto &\left\{J_{applied}(t) \times \left(N_{surf,intact}(t)\right)\right\} \ ... \\ &...+ \left\{J_{applied}(t) \times \left(N_{surf,fracture}(t) + N_{vol,fracture,e}(t)\right)\right\}\end{aligned} \tag{2.25}$$

Thus, for mass conservation to be satisfied, the amount of lithium entering through the flux acting on the microcrack-electrolyte interface, must be equal to the net amount of lithium generated/consumed by the volumetric electrochemical reaction terms.

$$J_{applied}(t)\times\left(N_{surf,fracture}(t)+N_{vol,fracture,e}(t)\right)=J_{gen}(t)\times\sum_{CV}\text{Volume} \qquad (2.26)$$

where $\sum_{CV}\text{Volume}$ is the summation of all the control volumes with electrochemically active microcracks.

Thus, the magnitude of the electrochemical reaction terms $\left(J_{gen}(t)\right)$ is given by equation (2.27).

$$J_{gen}(t)=J_{applied}(t)\times\frac{\left(N_{surf,fracture}(t)+N_{vol,fracture,e}(t)\right)}{\sum_{CV}\text{Volume}} \qquad (2.27)$$

The flowchart displayed in fig.8 illustrates systematically the steps involved in the methodology.

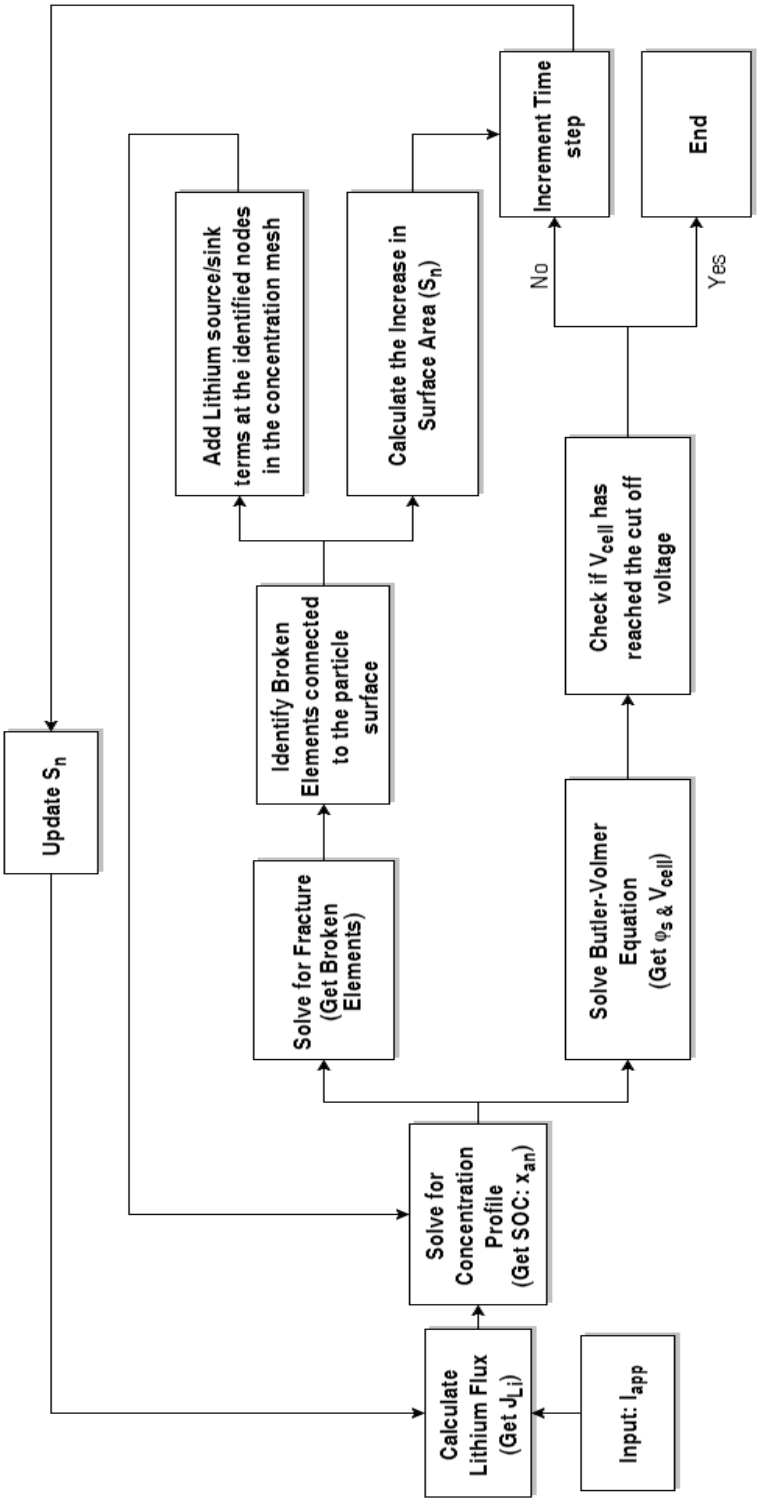

Figure 8: Model flowchart

The voltage of the cell is the difference between the solid state potentials between the electrodes which can be obtained from the overpotentials by solving the Butler-Volmer equation.

Table 1 enlists all the material parameters used for simulating the graphite anode.

Parameter Name	**Value**	**Units**
Diffusion coefficient (D_0)	3.9×10^{-14}	m^2/s
Diffusion expansion coefficient (ω)	1.14×10^{-6}	m^3/mol
Young's modulus (E)	70.57	GPa
Poisson's ratio (ν)	0.277	-
Mean fracture energy threshold per unit area (Ψ)	2	J/m^2
Maximum stoichiometric Li ion concentration (c_{max})	31833	mol/m^3

Table 1: Material parameters for simulations

CHAPTER III

SINGLE DISCHARGE

Majority of the mechanical degradation observed in LIB electrodes occurs during the first cycle. The incremental damage decreases significantly in the subsequent cycles [40, 60]. After the first few cycles, it is observed that the mechanical degradation in electrodes completely saturates. Hence, to study the evolution of microcracks in the LIB electrodes, it is crucial to pay special attention to the mechanical behavior of electrodes in the first cycle. This chapter is dedicated to the study of mechanical degradation during the first discharge cycle.

Unlike the Single Particle Model, the model developed here has electrochemical area of the electrode varying depending on the nature and magnitude of the microcracks formed in the active particles. Microcrack formation from the surface of the particle contributes to an increase in electrochemical area by introducing new solid particle – electrolyte interface where electrochemical reactions can take place. For a constant current cycle, this implies a proportionate decrease in lithium flux. Hence, on one hand, the electrochemical reactions lead to mechanical degradation by formation and propagation of microcracks in the active particles while on the other hand, these microcracks in turn directly affect the electrochemical reactions by providing more area for the electrochemical reactions to take place thereby reducing the lithium flux. To be able to illustrate this intimate two-way coupling between the mechano-electrochemical

phenomena observed in the LIB electrodes and to predict its effect on the cell performance is the main focus of this chapter.

Single Particle Model is widely accepted by the scientific community as a model that simulates the ideal case battery behavior as it does not account for mechanical degradation in the active particles. Many interesting distinctions can be made by comparing the model developed here with the Single Particle Model. Later in this chapter, such comparison is made highlighting the effect of mechano-electrochemical coupling.

Towards the end of this chapter, the influence of various factors on the mechanical degradation behavior and performance of LIBs is studied. Active particle size, rate of discharge and temperature are some of the factors that are investigated and a mechanical degradation phase map is developed to act as a guideline in selecting the best values for the influencing factors.

To begin with, a representative simulation for the discharge process of an anode particle is presented. Following are the battery/operating parameters for the representative simulation:

- Radius of Active Particle = 12.5 μm
- Temperature = 25°C
- Rate of Discharge = 2C

Fig. 9 shows the fracture density evolution with time. In the early stages of the discharge process, a steep increase in the fracture density can be observed. The incremental growth in fracture decreases towards the end of the discharge process. For the representative case, 12.9% of the spring elements are fractured by the end of the discharge cycle.

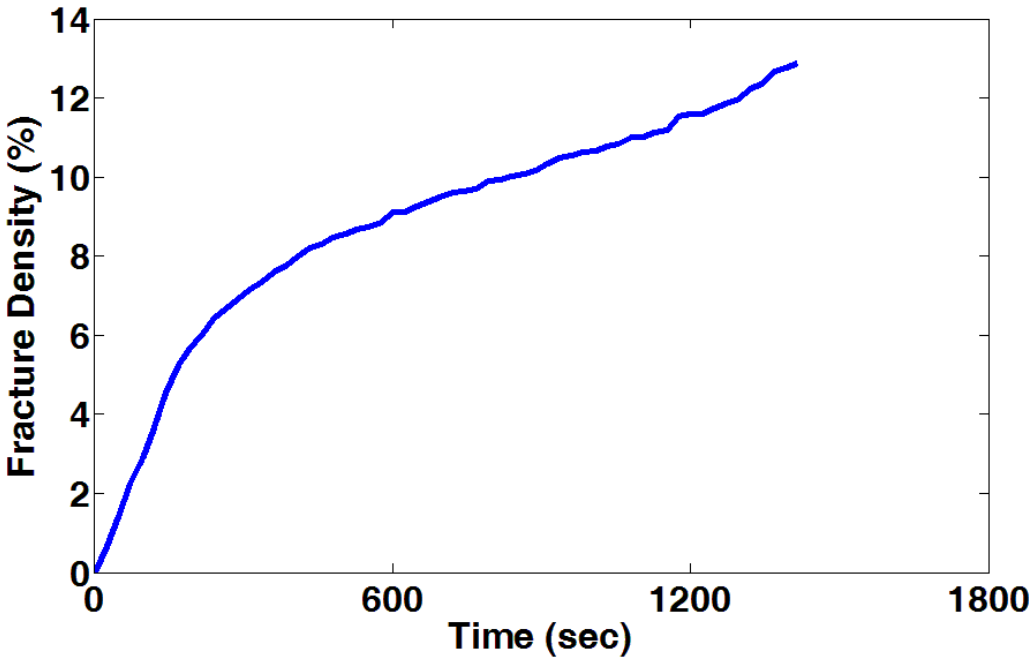

Figure 10: Evolution of fracture density (%)

To investigate the nature of microcrack propagation, the broken spring elements are plotted for 4 different time instances during the discharge process in fig. 10. As discussed earlier, the microcrack chains formed by the broken elements may or may not be exposed to the electrolyte depending on whether the chains emanate from the surface of the particle or not. In fig.10, the microcracks denoted by red colored markers are linked to the surface of the particle and are hence exposed to the electrolyte making them electrochemically active whereas the microcracks denoted by the black colored markers are isolated and electrochemically inactive. One key observation that can be made from the fig. 10 is that the microcracks are not uniformly distributed throughout the surface of the particle. The electrochemically active microcracks are preferentially propagated over the isolated microcracks due to the occurrence of electrochemical reactions at the electrochemically active microcrack-electrolyte interfaces. Thus the electrochemical reactions considerably affect the mechanical degradation behavior observed in the electrodes. This is evident from the long radial microcracks observed at the end of discharge in fig. 10.

Figure 11 shows the evolution of electrochemical area with time for the anode active particle. The growth of microcracks in the active particle directly affects the electrochemical area. All the electrochemically active microcracks increase the available area for electrochemical reactions leading to an increase in the electrochemical area of the cell. But as the discharge cycle progresses, certain regions within the anode active particle can get depleted of lithium even before the discharge cycle ends. Such regions are then assumed to not participate in the electrochemical reactions anymore and are thus called

ineffective. Thus, even though the solid particle-electrolyte interfacial area monotonically increases with time, the effective electrochemical area exhibits a maxima post which it decreases. This behavior is exhibited in fig. 11. Initially, the anode active particle has enough lithium throughout the particle for the electrochemical reactions and thus the ineffective area is zero. However, as lithium is being consumed, the ineffective area increases. The electrochemical areas mentioned above are related by equation 2.27.

Figure 11 shows the evolution of electrochemical area with time for the anode active particle. The growth of microcracks in the active particle directly affects the electrochemical area. All the electrochemically active microcracks increase the available area for electrochemical reactions leading to an increase in the electrochemical area of the cell. But as the discharge cycle progresses, certain regions within the anode active particle can get depleted of lithium even before the discharge cycle ends. Such regions are then assumed to not participate in the electrochemical reactions anymore and are thus called ineffective (see fig. 13). Thus, even though the solid particle-electrolyte interfacial area monotonically increases with time, the effective electrochemical area exhibits a maxima post which it decreases. This behavior is exhibited in fig. 11. Initially, the anode active particle has enough lithium throughout the particle for the electrochemical reactions and thus the ineffective area is zero.

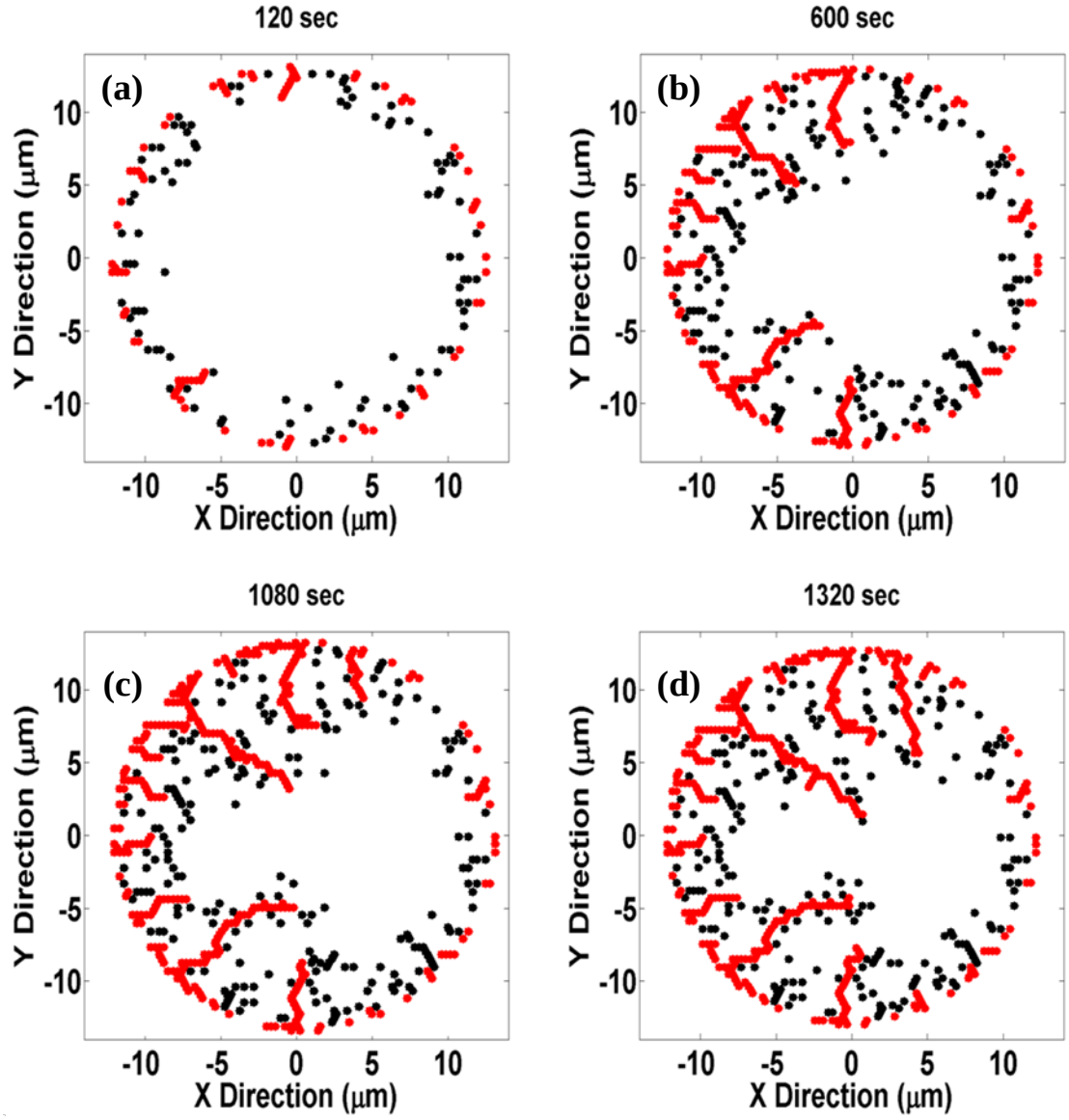

Figure 11: Distribution of electrochemically active (red colored) and inactive microcracks (black colored) at (a)120 sec (b) 600 sec (c) 1080 sec (d) 1320 sec – end of discharge

However, as lithium is being consumed, the ineffective area increases. The electrochemical areas mentioned above are related by equation 2.28.

$$A_e^{tot} = A_e^{eff} + A_e^{ineff} \tag{2.28}$$

During the cycle, the area increases to around twice the initially value while it ends at the point when the effective electrochemical area is around one fourth of the initial value. Hence, the area drastically changes during the cycle.

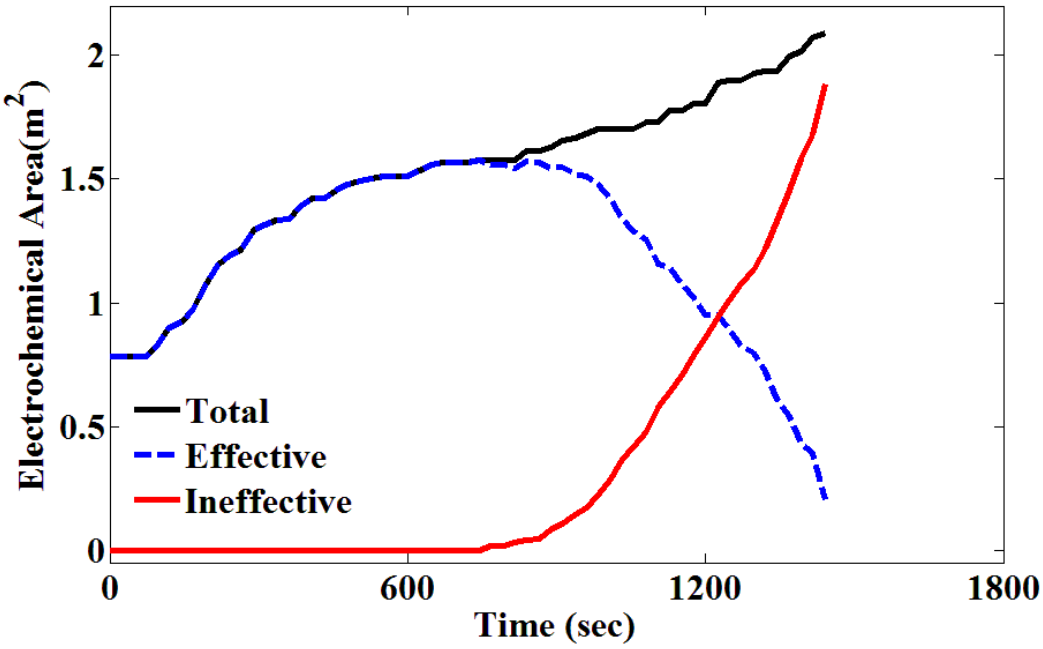

Figure 12: Evolution of effective, ineffective and total electrochemical area of the electrode

The two way mechano-electrochemical coupling in the active particle is highlighted by concentration contour plots shown in fig. 12. Microcracks are superimposed on the contour plots. The formation and propagation of microcracks influences the concentration distribution significantly which in turn affects the microcrack

propagation. The reactions taking place in the electrochemically active microcracks consume lithium. This locally decreases the lithium concentration in the proximity of the electrochemically active microcracks thereby increasing the concentration gradient. This leads to higher diffusion induced stress leading to further propagation of the microcracks; repeating the cycle.

Unlike the observations made from the Single Particle Model, the concentration distribution within the active particle predicted by the model developed here is not uniform in the azimuthal direction. This phenomenon is evident from the contour plots shown in fig. 12. Further, since the surface area of the particle and the microcrack-electrolyte interfacial areas are the locations where the reactions take place, these are the regions that are expected to get depleted of lithium earliest. Fig. 13 shows the concentration contour plots without electrochemically ineffective/inactive regions.

To study the effect of electrochemical reactions in the microcracks on the mechanical degradation, lithium concentration distribution and performance of the cell, in this section, comparisons have been made between the following models:

1. Single Particle Model – purely electrochemical model without mechanics
2. Mechanics model – where microcracks merely reduce the diffusivity but no electrochemical reactions take place in the microcracks
3. Mechano-Electrochemical model - has both mechanics as well as electrochemical reactions in microcracks

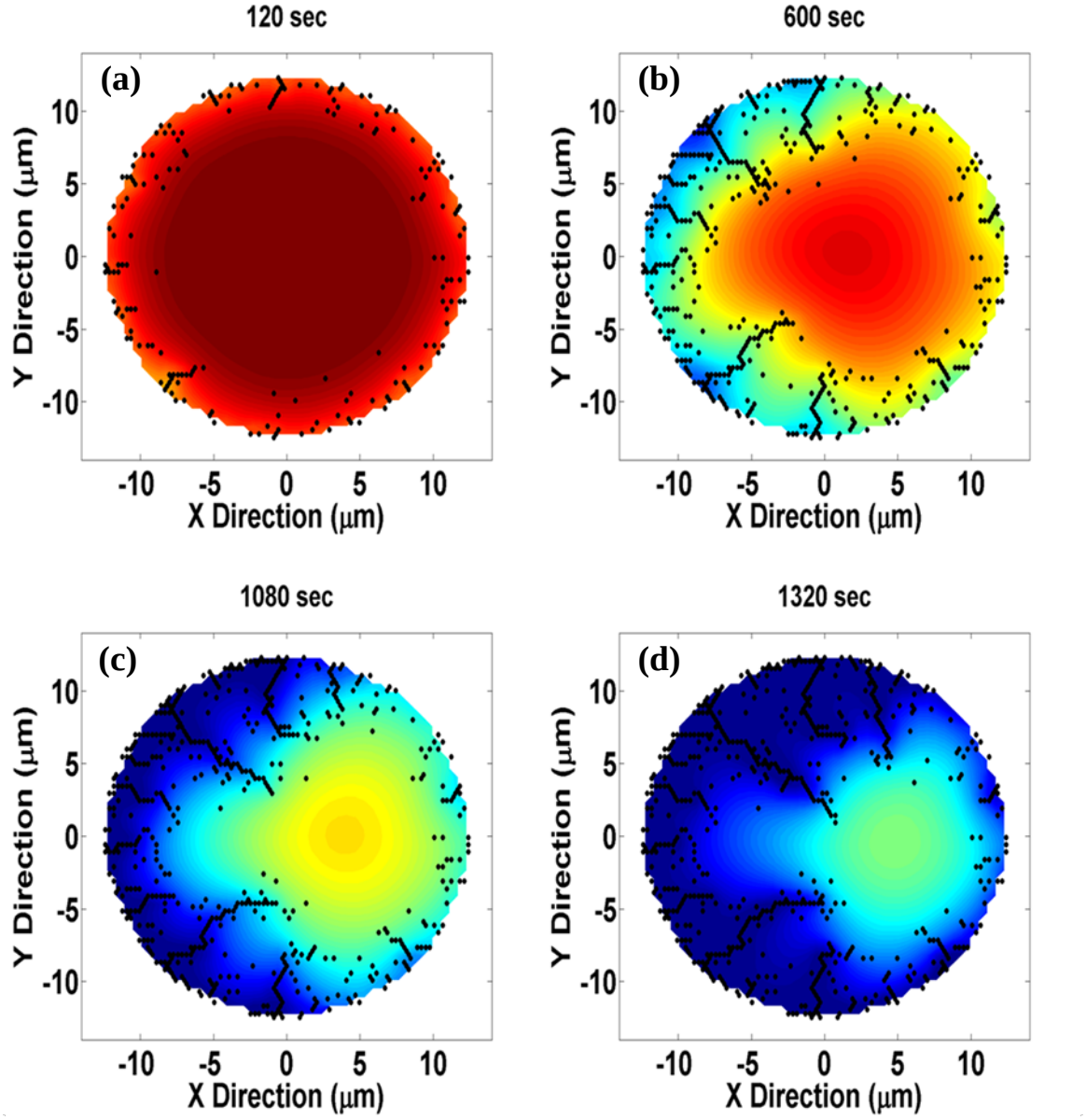

Figure 13: Concentration contour plot with superimposed microcracks at (a)120 sec (b) 600 sec (c) 1080 sec (d) 1320 sec – end of discharge

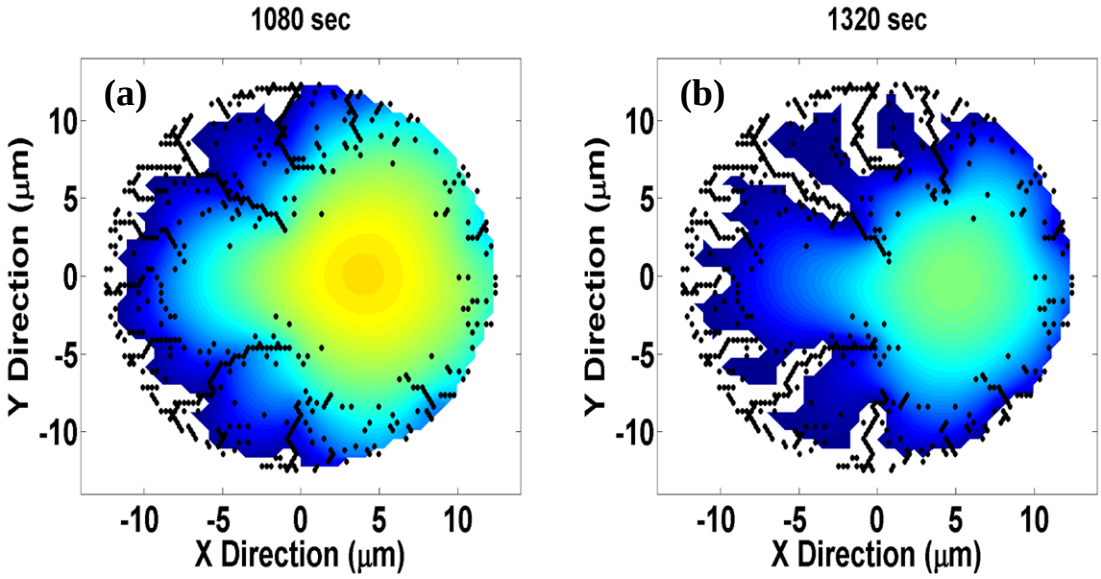

Figure 14: Concentration contour plots showing only the effective electrochemical area at (a) 1080 sec (b) 1320 sec – end of discharge

The Mechanics model predicts a higher fracture density at a given time compared to the Mechano-electrochemical model. This is intuitive as the mechanics model has a constant lithium flux throughout the discharge process while the mechano-electrochemical model has lithium flux value decreasing with increasing surface area. However, since the electrolyte does not percolate into the active particle through cracks in the mechanics model, the discharge simulation for mechanics model stops before that for the mechano-electrochemical model. And for the additional time that the mechano-electrochemical model takes to completely discharge, it surpasses the fracture density observed in the mechanics model.

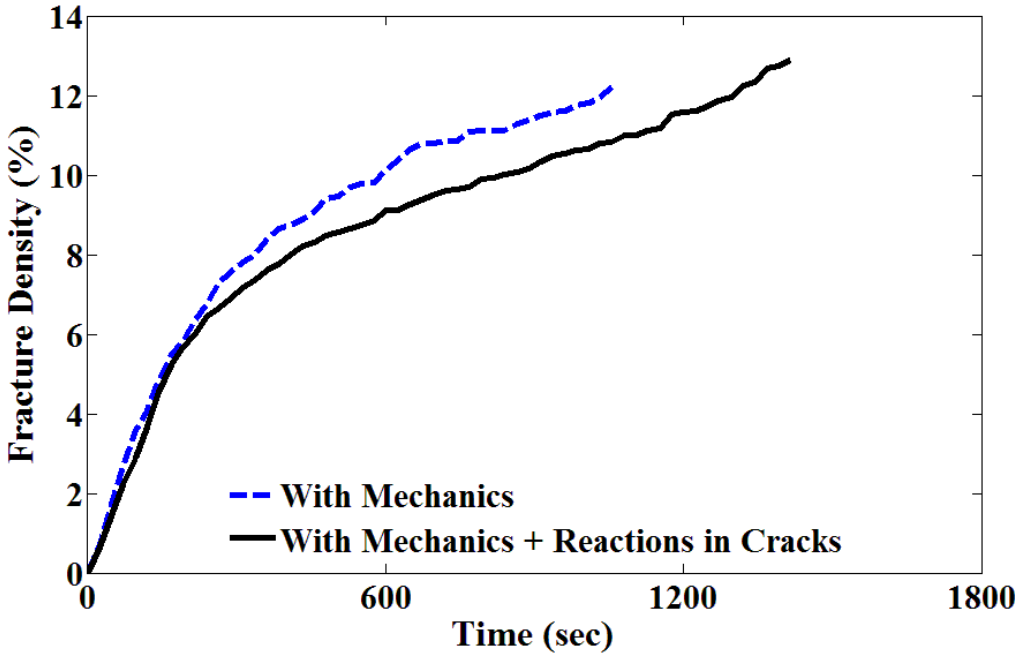

Figure 15: Model comparison – fracture density (%) evolution

One unique difference between the mechanics and the mechano-electrochemical model is the coupling between mechanical damage and electrochemical reactions. In mechanics model, the microcracks affect the concentration distribution only by reducing the local diffusivity of active material. This has a subtle effect on the lithium concentration distribution in the vicinity of the microcracks. In the mechano-electrochemical model, however, this coupling is more pronounced, as other than reducing the local diffusivity of active material, microcracks also result in new surfaces that participate in electrochemical reactions. This significantly changes lithium concentration in the vicinity of the microcracks. This difference is highlighted by fig. 15 that shows the concentration contour

plots for the two models at the end of discharge. Microcracks are superimposed upon the contour plots to give an idea of the extent of mechanical degradation. For the mechanics model, the microcracks are more uniformly distributed along the azimuthal direction whereas for the mechano-electrochemical model, the microcracks are directional and thus not uniformly distributed along the azimuthal direction. The directionality of microcrack propagation is due to the electrochemical reactions taking place at the microcracks that lead to preferential propagation of the microcracks further. Thus, as observed in fig. 15, microcracks grow radially very close to the center of the particle. In the mechanics model, however, the microcracks are unable to propagate that close to the center of the particle and are relatively shorter. This is reflected from the cumulative distribution of fracture density in the radial direction plotted in fig. 16. For the mechanics model, microcracks are formed only beyond a radial distance of 6.5 μm from the center of the particle. Thus, the region in the center of the particle, up to radius of 6.5 μm, is microcrack free. For the mechano-electrochemical model, microcracks can be observed beyond a radial distance of 1 μm from the center of the particle. Thus, the microcracks in the mechano-electrochemical model extend up to very close radial distances from the center of the particle.

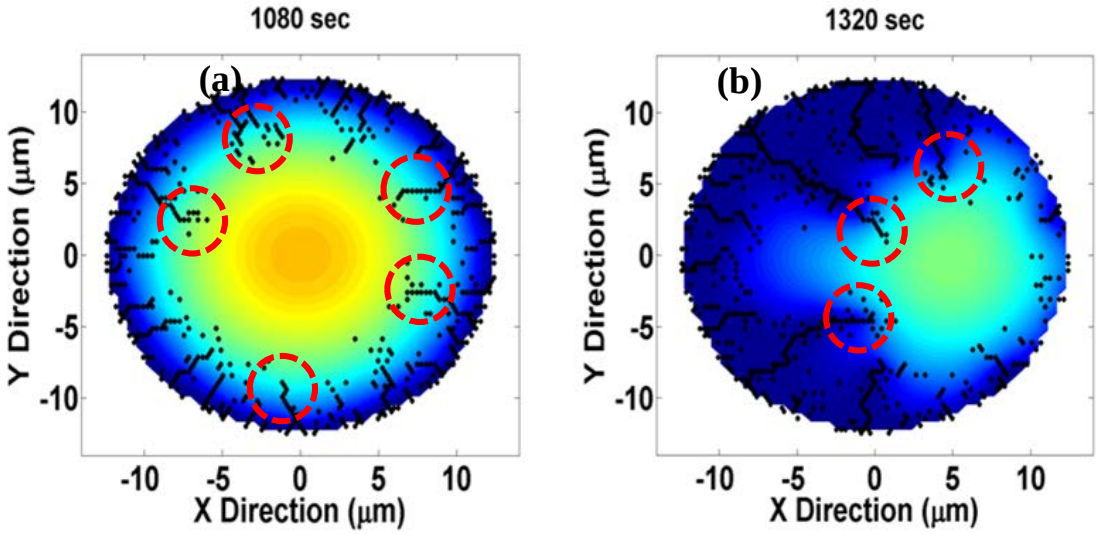

Figure 16: Model comparison - concentration contour plots with microcracks superimposed at the end of discharge
(a) with mechanics (b) with mechanics + reactions in cracks

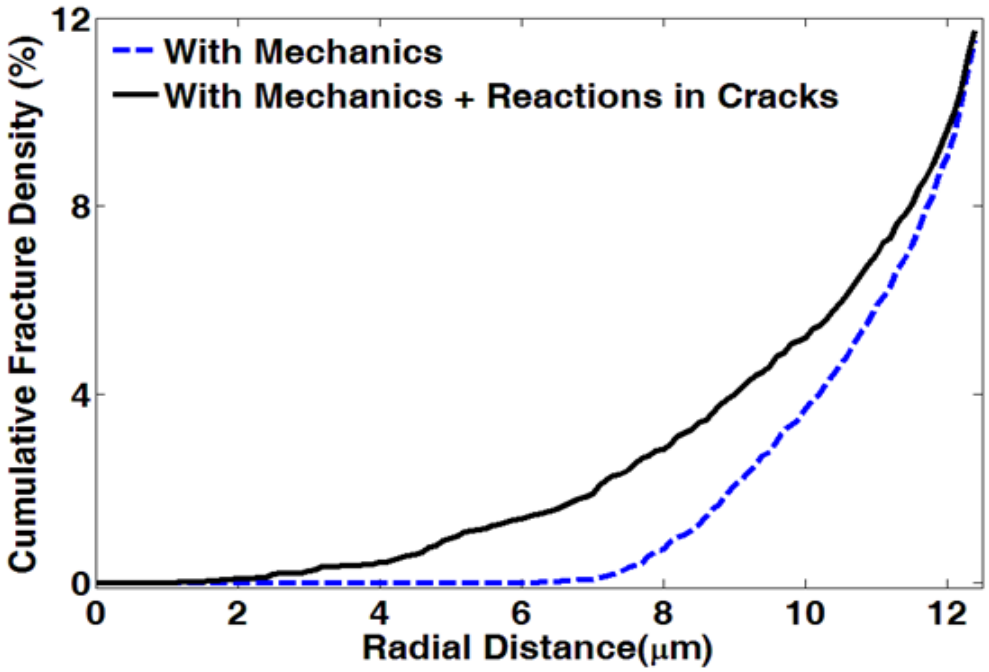

Figure 17: Model comparison - radial distribution of fracture density (%) at the end of discharge

This distinction can also be highlighted by plotting the angular distribution of lithium concentration and normalized fracture density. In fig. 17, the above mentioned angular distributions are plotted on a polar plot for the two models. It can be inferred from this plot that at the end of discharge, the concentration distribution and microcrack distribution is almost uniform along the azimuthal direction for the mechanics model. This is not the case for the mechano-electrochemical model. The fracture density is maximum in the 2nd and 3rd quadrant however, lithium concentration is maximum for the 1st and 4th quadrant. This non-uniform angular distribution of lithium concentration and fracture density is a result of the intimate two-way coupling between mechanics and electrochemistry. Fracture density being maximum in the 2nd and 3rd quadrant implies that these regions have maximum electrochemical area for reactions. Thus, more lithium is extracted by the electrochemical reactions reducing the lithium concentration in these quadrants.

For the single particle and mechanics model, the electrochemical area is not affected by fracture growth and hence is constant till regions within the particle start getting depleted of lithium. For the mechano-electrochemical model, as discussed earlier, the area initially increases due to fracture growth. For all of the models, once regions within the particle start getting depleted of lithium, the effective electrochemical area plunges significantly (see fig. 18).

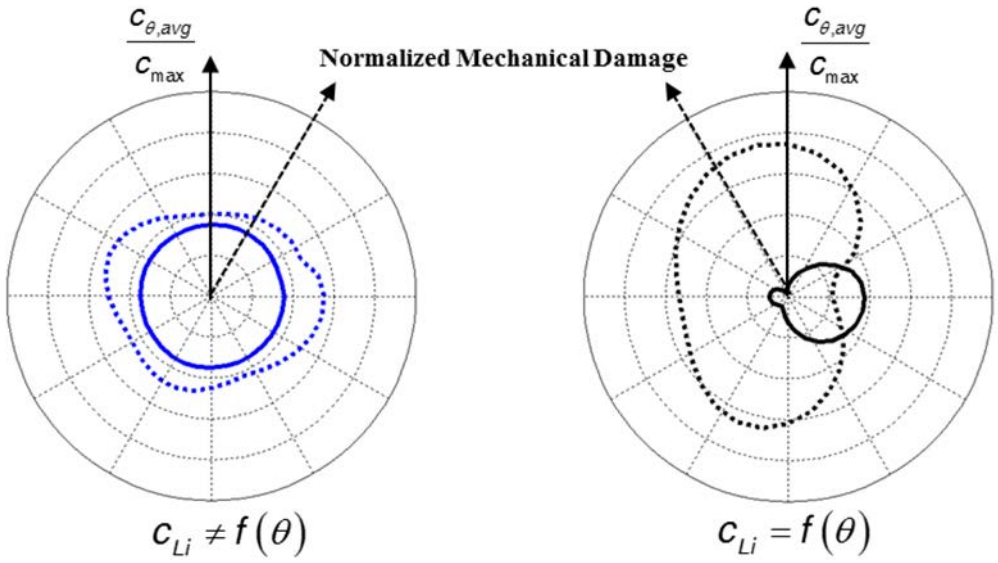

Figure 18: Model comparison - angular distribution of average lithium concentration and fracture density at the end of discharge (a) with mechanics (b) with mechanics + reactions in cracks

**Solid lines represent Li concentration distribution*
**Dashed lines represent fracture density distribution*

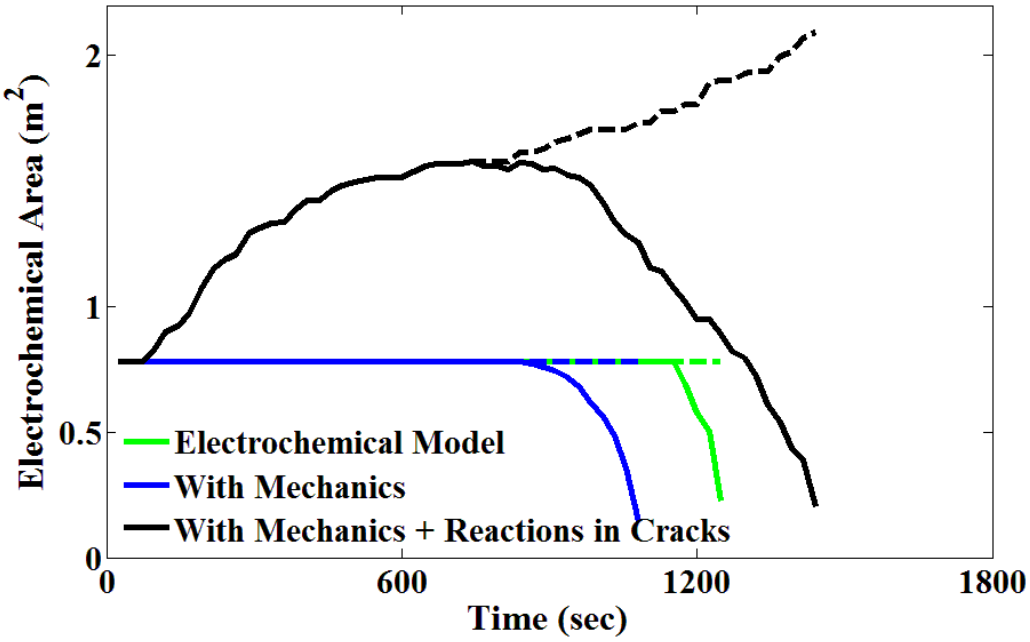

Figure 19: Model comparison - electrochemical area evolution

In the lithium ion battery literature, the single particle model is considered the ideal case where the performance is just electrochemically limited. Until now, all the computational models developed to investigate the mechanical degradation behavior of the electrodes accounted only for the negative effect of mechanical degradation like by decreasing the diffusivity in the proximity of the microcracks. Thus the performance predicted by all of the mechanical degradation models is lower than that predicted by the single particle model. But if electrochemical reactions in the microcracks are account for in modelling mechanical degradation, then this may not be necessarily true. The performance curves for the single particle model, mechanics model and mechano-electrochemical model are superimposed in fig. 19. As expected, at 2C discharge, the capacity predicted by the mechanics model is lower than that predicted by the single particle model. However, the mechano-electrochemical model predicts maximum capacity, even higher than the ideal case of single particle model. This might not be obvious at first but upon further scrutiny, this can be justified by comparing the effective diffusion lengths for the models. Since the single particle model and the mechanics model have the electrochemical reactions taking place only at the surface of the active particle, the lithium at the core of the active particle must diffuse radially outward to the surface of the particle. Hence, the diffusion length is constant for these models and is equal to the radius of the particle (R). For the mechano-electrochemical model, however, the electrochemical reactions take place not only at the surface of the particle but also at electrochemically active microcracks. This reduces the diffusion length for the mechano-electrochemical model as the lithium at the core of the particle now need not diffuse all

the way to the surface of the particle. The long radial cracks observed in the particle shown in fig. 15 indicate that the diffusion lengths are significantly reduced as microcracks form and propagate. This can be termed as the positive effect of mechanical degradation. The long radial electrochemically active microcracks help in extracting maximum lithium from the particle. This is reflected in the higher capacity predicted by the mechano-electrochemical model (fig. 19).

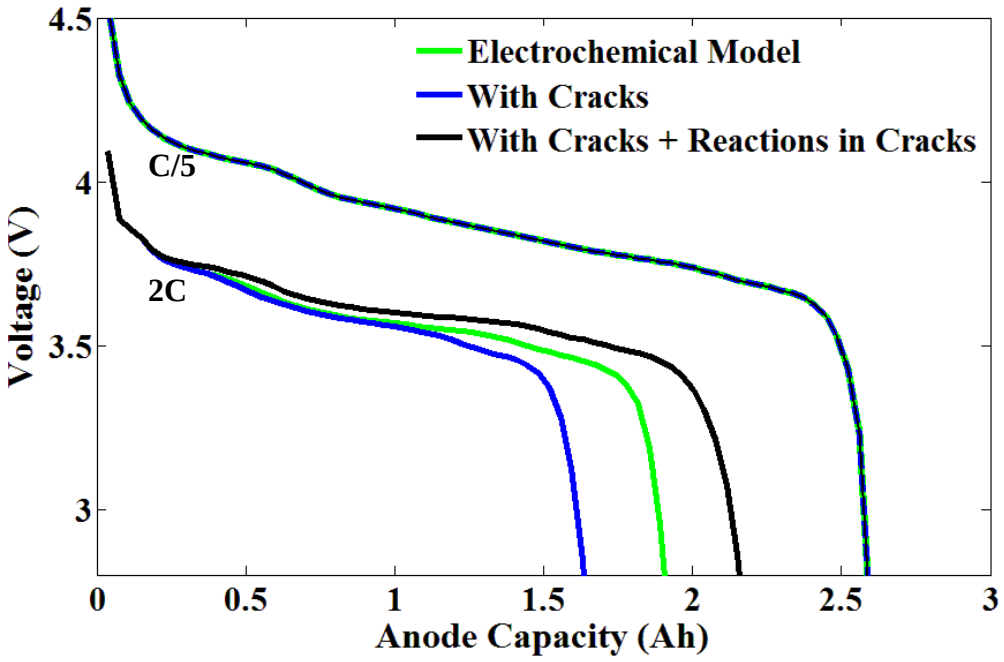

Figure 20: Model comparison - performance

Hence, more the mechanical degradation, longer are the microcrack chains, smaller is the effective diffusion length. Thus, at very low C-rates, there is enough time for diffusion to take place, minimizing the concentration gradients that are responsible for

mechanical degradation. Hence, at C/5 discharge, where negligible microcrack formation takes place, the performance predicted by the single particle, mechanics and mechano-electrochemical model overlap completely and thus are exactly the same (see fig. 19).

Effect of discharge rate

The extent of mechanical degradation occurring in the active particles depends on the rate at which the cell is being discharged. With increasing C-rate, the concentration gradient within the particle and hence, the diffusion induced stress increases. Thus, more mechanical degradation is expected to be observed in active particles undergoing discharge at higher C-rate. Fig. 20 shows mechanical degradation quantified using the fracture density for active particles for 5 different C-rate. At very low C-rate, the rate of electrochemical reactions is very low, allowing sufficient time for diffusion to take place and reduce the concentration gradient. Hence, negligible mechanical degradation can be observed at very low C-rate. As C-rate increases, the rate of electrochemical reactions taking place at the solid particle- electrolyte interface increases. If diffusion cannot cope up with the increase in the rate of reactions, high concentration gradients develop within the particle. Concentration gradients lead to a high diffusion induced stress within the particle increasing the chances of spring elements failing thereby increasing mechanical degradation observed in the particle. This trend can be seen in the fig. 20 that plots the fracture density versus normalized time (simulation time divided by the max. discharge time expected at that C-rate) for C/5, C/2, 1C, 2C and 5C discharge. The microcracks

directly affect the electrochemical area of the electrode. The evolution of effective electrochemical area for the same five discharge rates is shown in fig. 21. Initially all the cases have same electrochemical area. However, with time, for higher C-rate (5C & 2C), the effective electrochemical area rises significantly while for lower C-rate (C/5 & C/2) it remains constant.

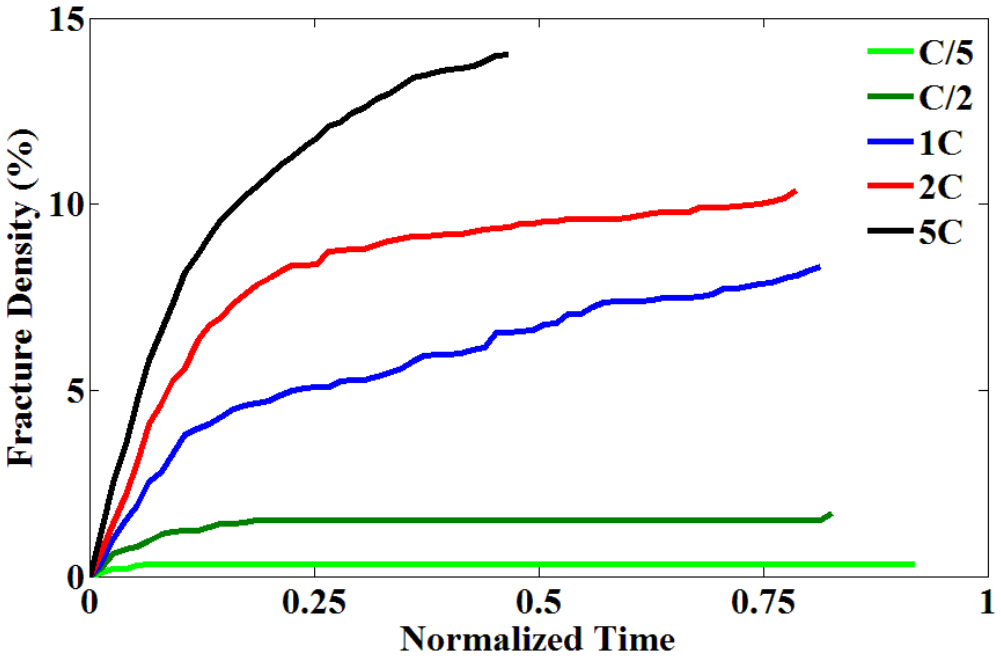

Figure 21: Effect of rate of discharge – fracture density

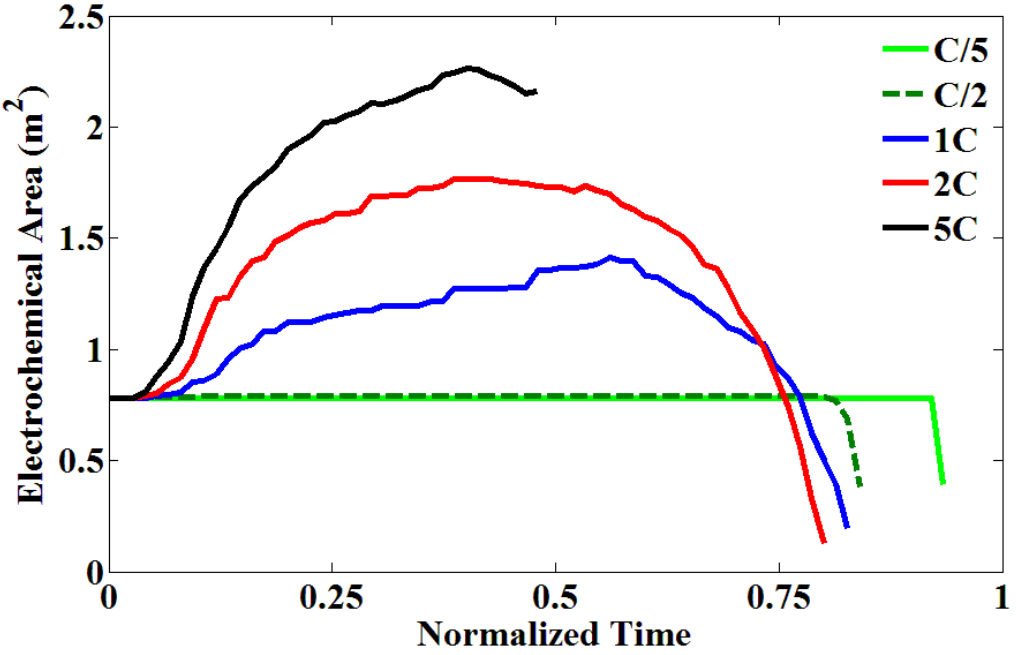

Figure 22: Effect of rate of discharge – electrochemical Area

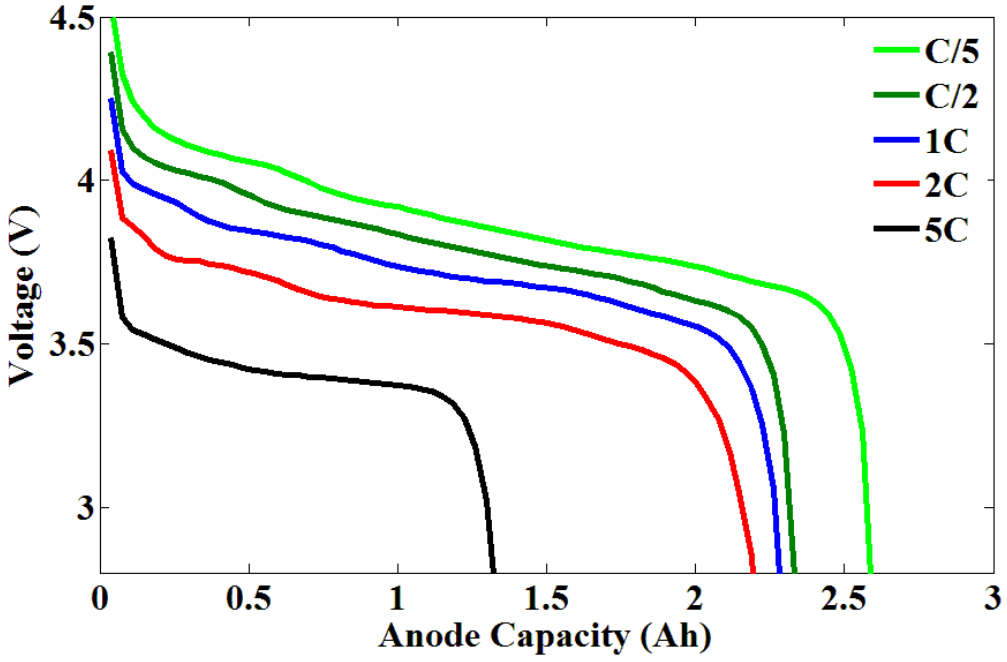

Figure 23: Effect of rate of discharge – performance

As far as performance is concerned, the effect of C-rate on the observed cell capacity is as expected – lower the rate of discharge, more the capacity achieved. This is because at high C-rates, diffusion rate limits the maximum capacity that can be extracted from the cell. Thus, the observed capacity significantly reduces as the rate of discharge is changed from C/5 to 5C with C/5 case having roughly twice the capacity observed in 5C case (see fig. 22).

Effect of particle size

The size of active particle greatly influences the mechanical degradation observed in the particle. For the active particle to function, lithium within the particle must react with the electrolyte. Hence, the lithium stored in the active particle must diffuse through the particle to reach the active particle-electrolyte interface. The diffusion length scale can be thought of being approximately equal to the radius of the particle. For smaller particles, the length scale is short enough to develop a substantial concentration gradient. For larger particles, however, the diffusion length is large and so is the concentration gradient developed during discharge. As discussed earlier, this results in higher diffusion induced stresses and more mechanical degradation.

For investigating the effect of particle size, five cases with varying particle radius (5 μm, 7.5 μm, 10 μm, 12.5 μm and 15 μm) are simulated. For the simulations, every other operating/battery parameter is kept constant. Fig. 23 shows the fracture density versus

time for the five cases. As expected, at any given time during the discharge process, larger particles have more fractures than smaller ones. At the end of discharge process, the 15 µm particle has a fracture density of around 9% while the 5 µm particle has negligible fracture density. Following the trend observed in fracture density, the 5 µm particle has a constant electrochemical area until the start of lithium depletion in specific regions within the particle at the end of the discharge cycle (see fig. 24). However, the electrochemical area for larger particles increases with the discharge process until lithium depletion kicks in.

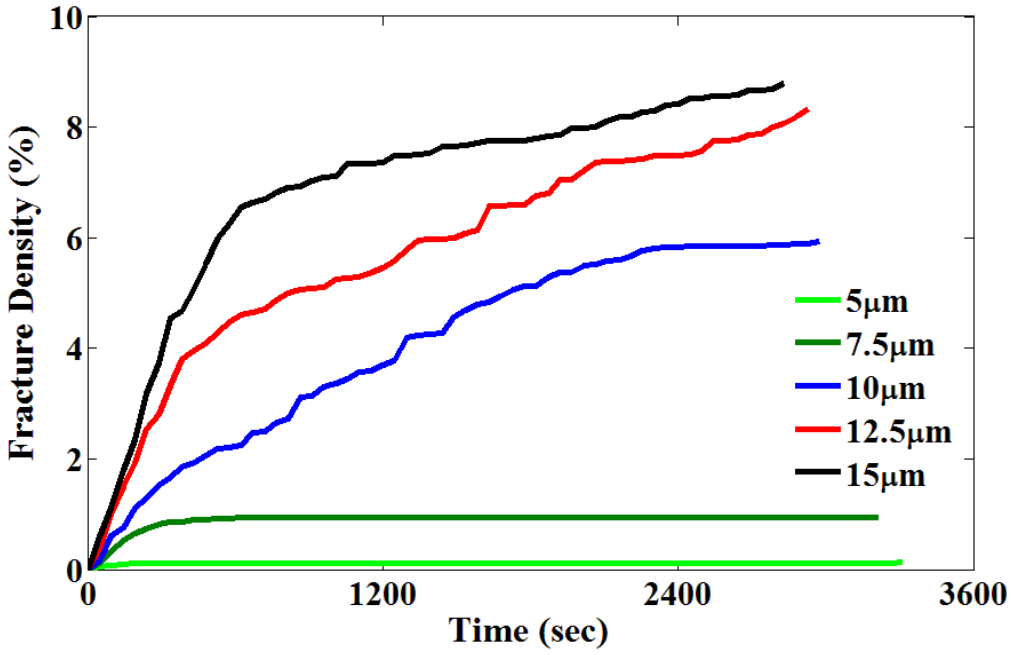

Figure 24: Effect of particle size – fracture density

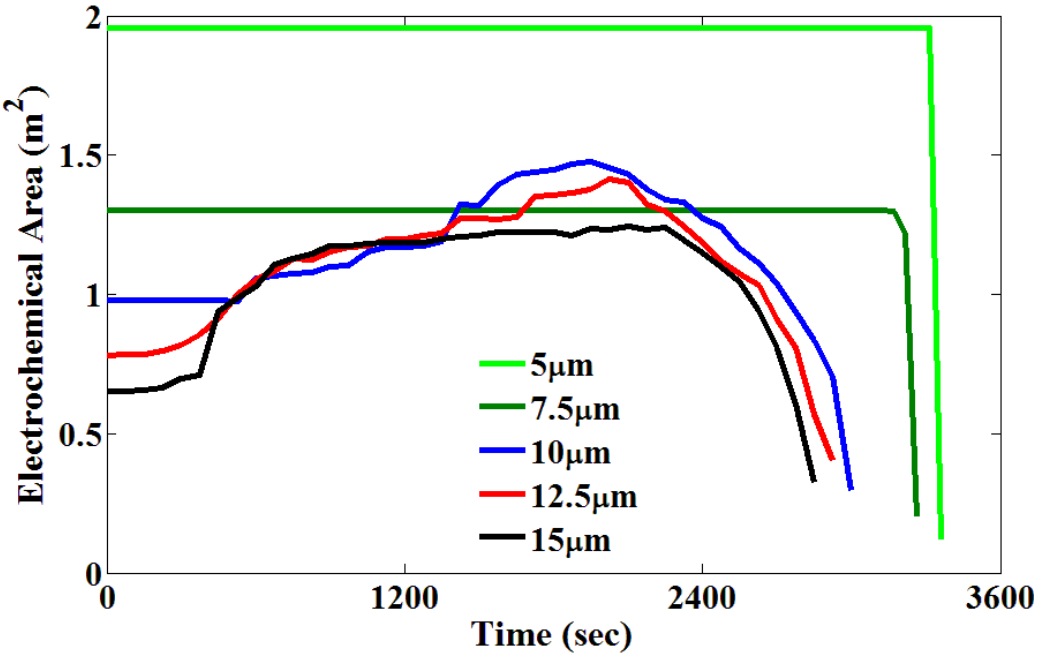

Figure 25: Effect of particle size – electrochemical area

Performance predicted using the mechano-electrochemical model for the five cases is shown in fig.25. Lower resistance to diffusion in smaller particles leads to better utilization of the lithium in active particle giving higher cell capacity. Higher mechanical degradation observed in larger particles, imply presence of long radial microcracks in the particle. These microcracks tend to reduce the effective diffusion length by allowing for electrochemical reactions throughout their interface with the electrolyte. But since only few long electrochemically active microcracks are observed to have developed, the effect of increase in the radius dominates over the presence of longer microcracks resulting in a net increase in diffusion length scale, reflected in the reduction of capacity for larger particles as shown in fig. 25.

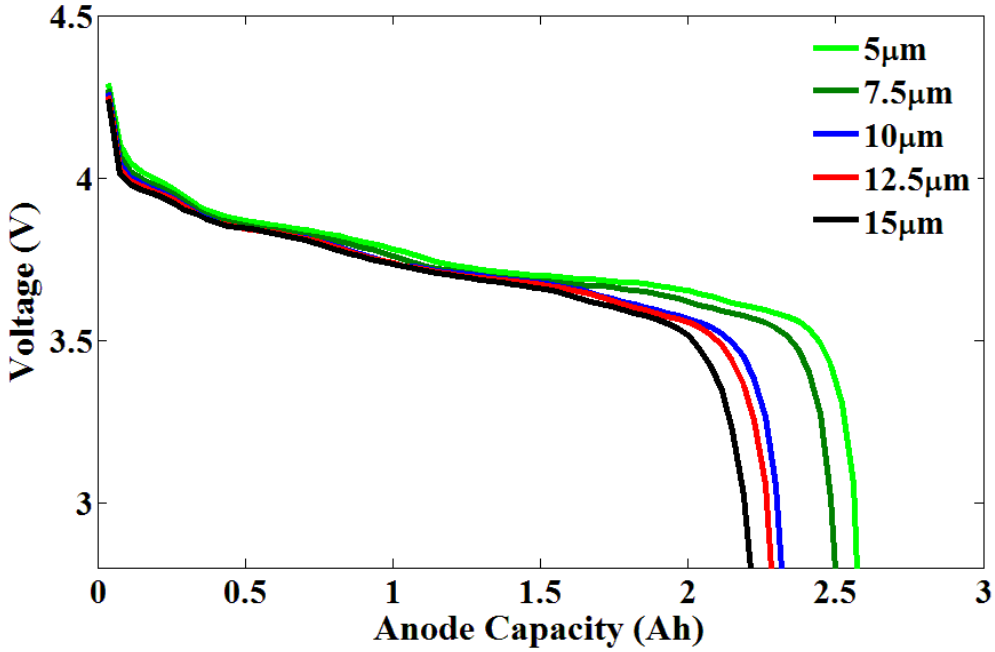

Figure 26: Effect of particle size – performance

Effect of temperature

Temperature can affect a cell in multiple ways. Temperature directly affects the diffusion of lithium inside the active particle by changing diffusion coefficient. Also, as the open circuit potential and overpotential are highly sensitive to temperature changes, temperature greatly affects the cell performance.

Temperature dependence of the diffusion coefficient in solids can be well captured by the Arrhenius equation [64]. Thus, diffusion coefficient reduces exponentially with temperature. Fig. 26 exhibits the variation of diffusion coefficient normalized by the diffusion coefficient at reference temperature of 25°C with temperature. The exponential

dependence on temperature makes diffusion coefficient very sensitive to temperature changes. For example, the diffusion coefficient at 50°C is approximately 11 times higher than the value at 0°C. Such sharp differences in the diffusion coefficient can have drastic repercussions on the mechanical degradation observed in the active particles.

$$\frac{D}{D_0} = \exp\left(\frac{E_a}{R}\left(\frac{1}{T_{ref}} - \frac{1}{T}\right)\right) \tag{2.29}$$

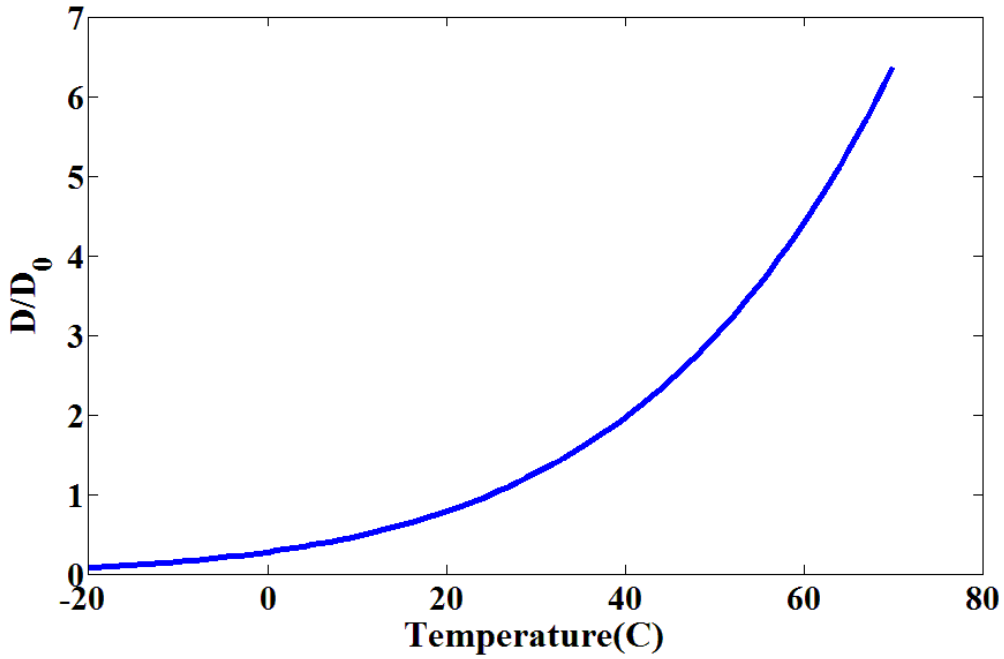

Figure 27: Effect of temperature – normalized Diffusivity (D/D_0)

Upon increasing temperature, diffusion coefficient increases facilitating the diffusion of lithium within the particle. This helps in reducing the lithium concentration gradient within the active particle. Thus, as temperature increases, lower mechanical

degradation is observed and better particle utilization is achieved. At lower temperatures, substantial concentration gradient exists within the particle leading to higher mechanical degradation. As can be seen from the fig. 27, the fracture density at the end of discharge at 0°C is 14.1% whereas at 50°C, the fracture density at the end of discharge is less than 1%.

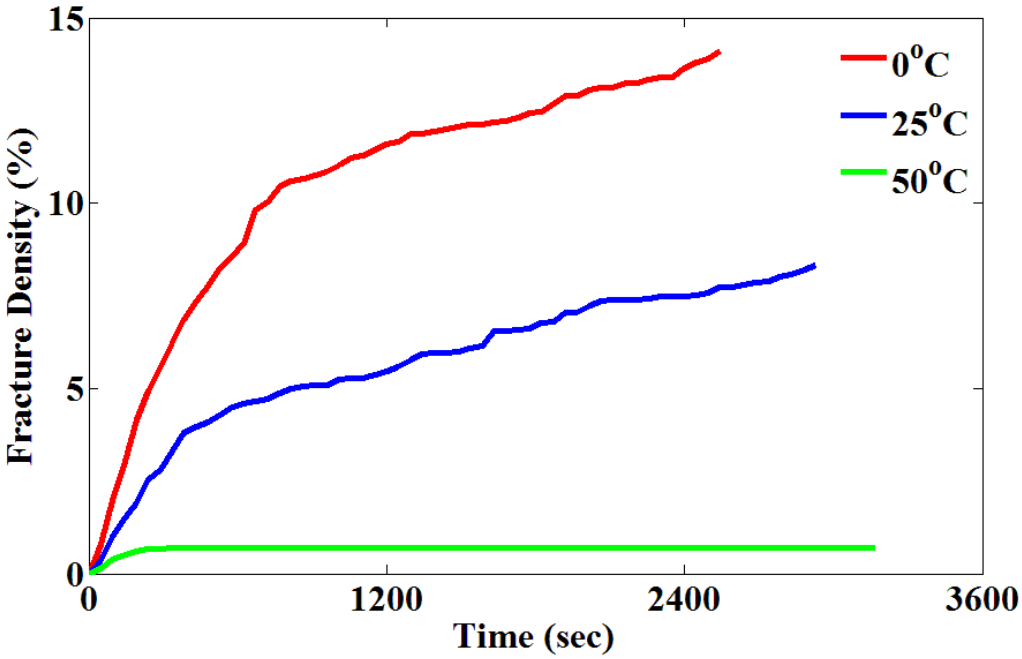

Figure 28: Effect of temperature – fracture density

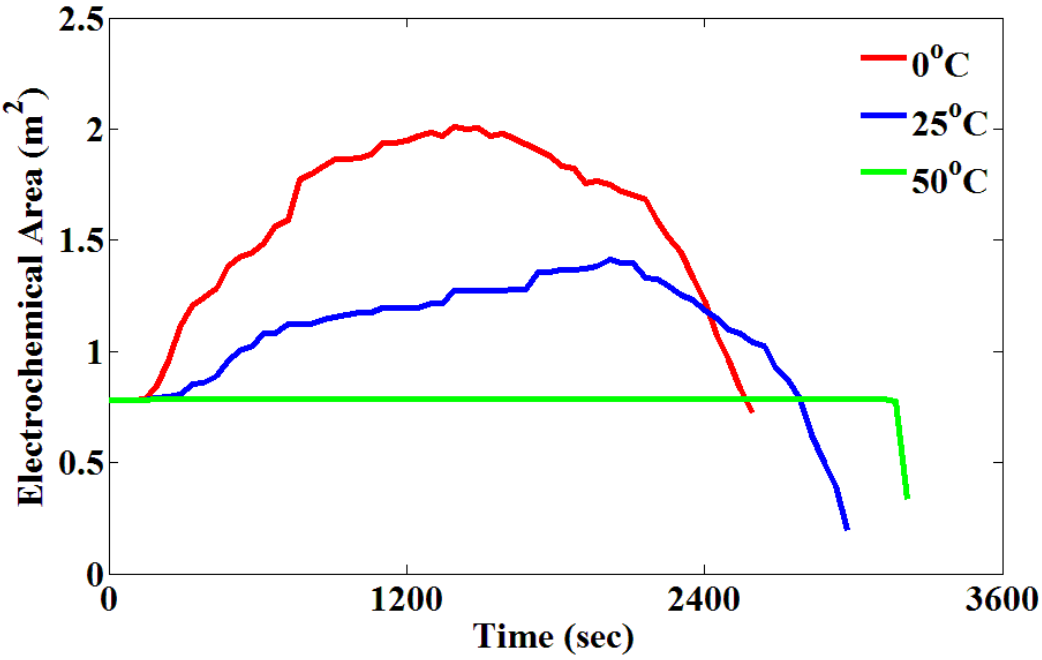

Figure 29: Effect of temperature – electrochemical area

Owing to extensive microcrack formation, a drastic increase in the electrochemical area can be observed at 0°C. The increase in electrochemical area at 50°C is negligible. Fig. 29 compares the performance curves obtained at 0°C, 25°C and 50°C. As higher temperatures lead to better utilization of the active particles, the cell capacity obtained at 50°C is very high. At 0°C, on one hand, increased microcrack formation leads to reduction in the effective diffusion length of the active particle, while on the other hand, the reduced diffusion coefficient decreases the rate of lithium diffusion. However, the reduction in diffusion coefficient dominates and slow diffusion of lithium limits the cell capacity to a lower value compared to that at ambient temperature (25°C).

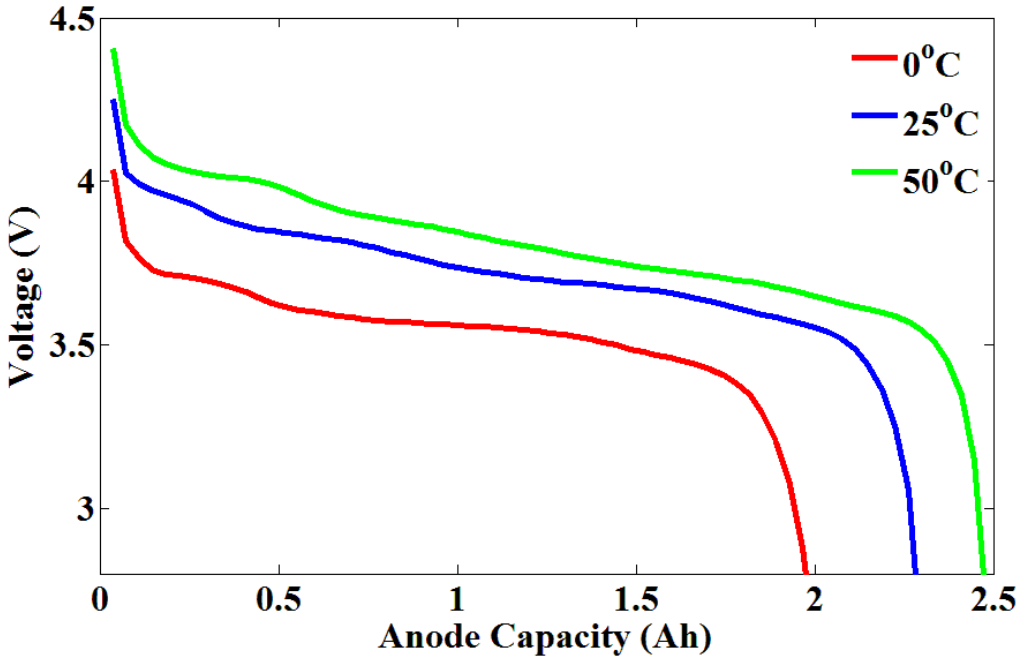

Figure 30: Effect of temperature – performance

It can be seen from the case studies discussed earlier that rate of discharge, particle size and temperature influence the behavior of cell significantly. Thus, it is necessary to carefully select the values of these influencing factors in order to optimize the cell performance. Depending on the case at hand, one or more of the influencing factors may not have much room for optimization and be fixed. For example, some applications of lithium ion battery require the battery to provide very high currents. Naturally, higher C-rate would imply greater concentration gradient within the particle, more mechanical degradation and limited utilization of cell capacity. However, the effect of higher C-rate can be reduced by tactfully choosing the other two influencing factors – particle size and temperature. From the case studies conducted earlier in this chapter, it was observed that

smaller particle radius reduces the diffusion length and higher operating temperature increases the diffusion coefficient; both resulting in faster diffusion of lithium within the particle, lower mechanical degradation and better utilization of cell capacity. Hence, for an application requiring high C-rate operation, choosing a battery with smaller particles and operating at higher temperatures within the allowable thermal window for the battery would enhance the battery performance.

Having said that, it will be beneficial to have a mechanical degradation phase map that can act as a guideline in thoughtfully selecting the influencing factors to optimize the cell performance depending on the specific conditions at hand. Fig. 30 shows the mechanical degradation phase map for three temperatures - 0°C, 25°C and 50°C. The phase maps show the extent of mechanical degradation expected at the end of first discharge cycle for different C-rate – particle size combinations.

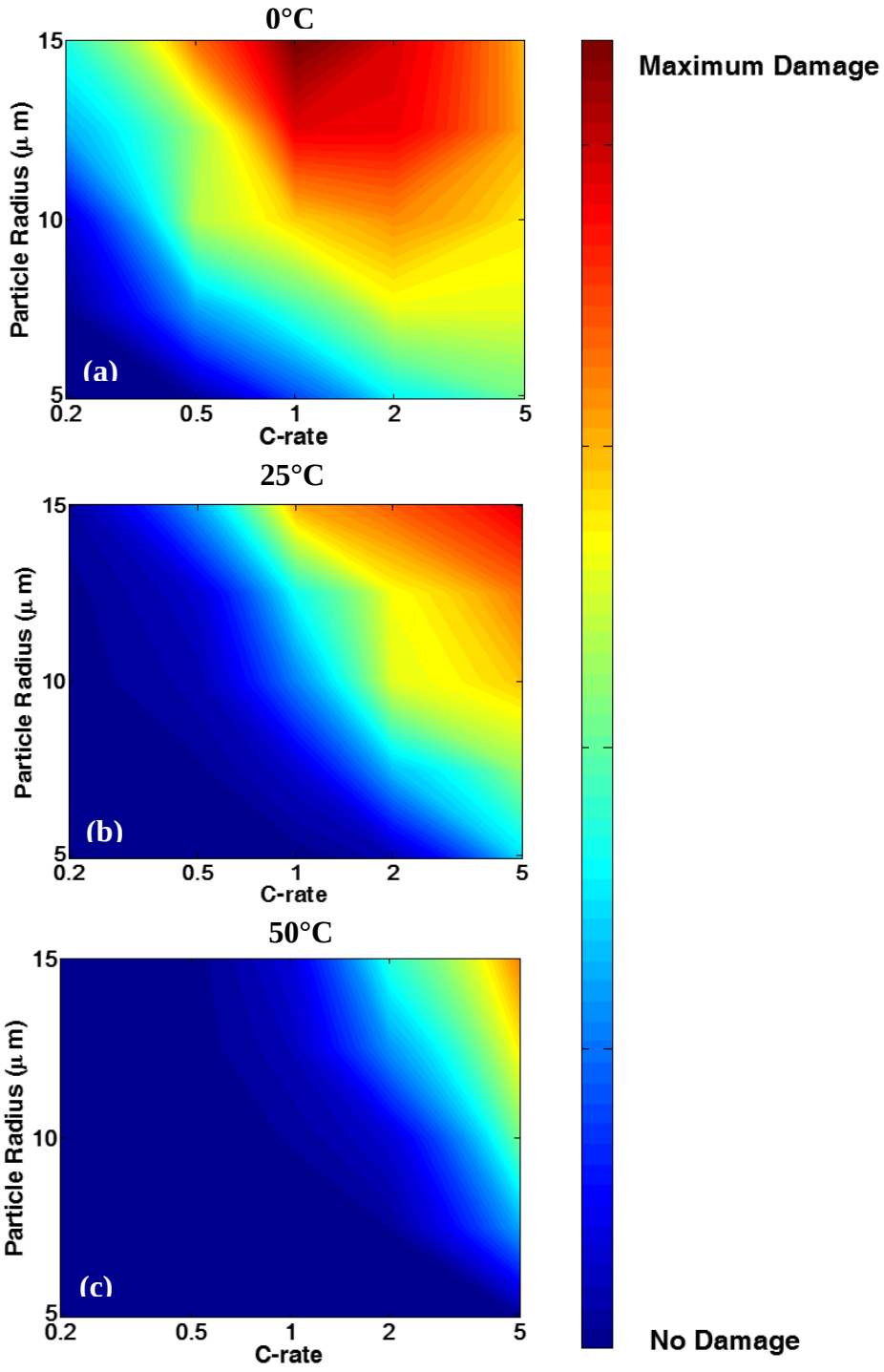

Figure 31: Mechanical degradation phase map for (a) 0°C (b) 25°C and (c) 50°C

CHAPTER IV

CYCLING BEHAVIOR

The lithium ion cells are expected to undergo multiple charge-discharge cycles during their usable life. Cycle life prediction of commercial LIB has been a key research topic lately. For that purpose, several degradation mechanisms that affect the cycle life of LIB are investigated [70-75]. In this chapter, the effect of cycling on mechanical degradation behavior of the electrodes is analyzed. As mechanical and electrochemical behaviors of the electrodes are deeply coupled, the mechanical degradation further affects electrochemical reactions for the subsequent time instances. Thus, investigating this two-way coupled behavior between the electrochemical and mechanical phenomena within the electrodes over multiple charge-discharge cycles is important for predicting the cycle life of LIB.

The results from single discharge highlight that the electrochemically active microcracks grow preferentially over the inactive microcracks. Such microcracks are found to emanate from the surface of the particle and extend radially towards the center. Over multiple charge-discharge cycles, it is possible that two or more microcrack chains can coalesce. This merging of microcracks can cause the active particle to disintegrate into many smaller particles. Connectivity of these smaller particles with the bulk of active material is dependent on their contact with conductive additives. There are high chances that some of these smaller particles have poor contact with the conductive additives rendering them ineffective to participate in subsequent lithiation-delithiation cycles.

In this chapter, we focus on the propagation of microcracks during constant current cycling. The corresponding evolution of electrochemical area is also studied. The influence of different physicochemical factors on the mechano-electrochemical behavior of cell during cycling is also studied.

Figure 31 and 32 shows the evolution of microcracks for a representative cycling simulation where a 12.5 μm particle is operated at 25°C and 1C current. From the figure, it is evident that during the initial cycles, the microcracks growth is fast and the chances of active particle disintegrating into smaller particles are high.

Figure 33 shows the concentration contours with superimposed microcracks at the end of 1st, 2nd, 3rd and 4th discharge half cycle. Majority of the microcracks are developed in the first cycle. The incremental microcrack formation in subsequent cycles decreases. Fig. 34 shows the fracture density evolution with charge-discharge cycles. It is clear from the figure that mechanical degradation is saturated by the end of the 4th cycle post which no microcracks are formed. This trend will also be reflected in the electrochemical area evolution of the electrode (see fig. 35). The spikes in the electrochemical area vs. cycle plot in fig. 34 are due to depletion of lithium from specific regions in the active particle.

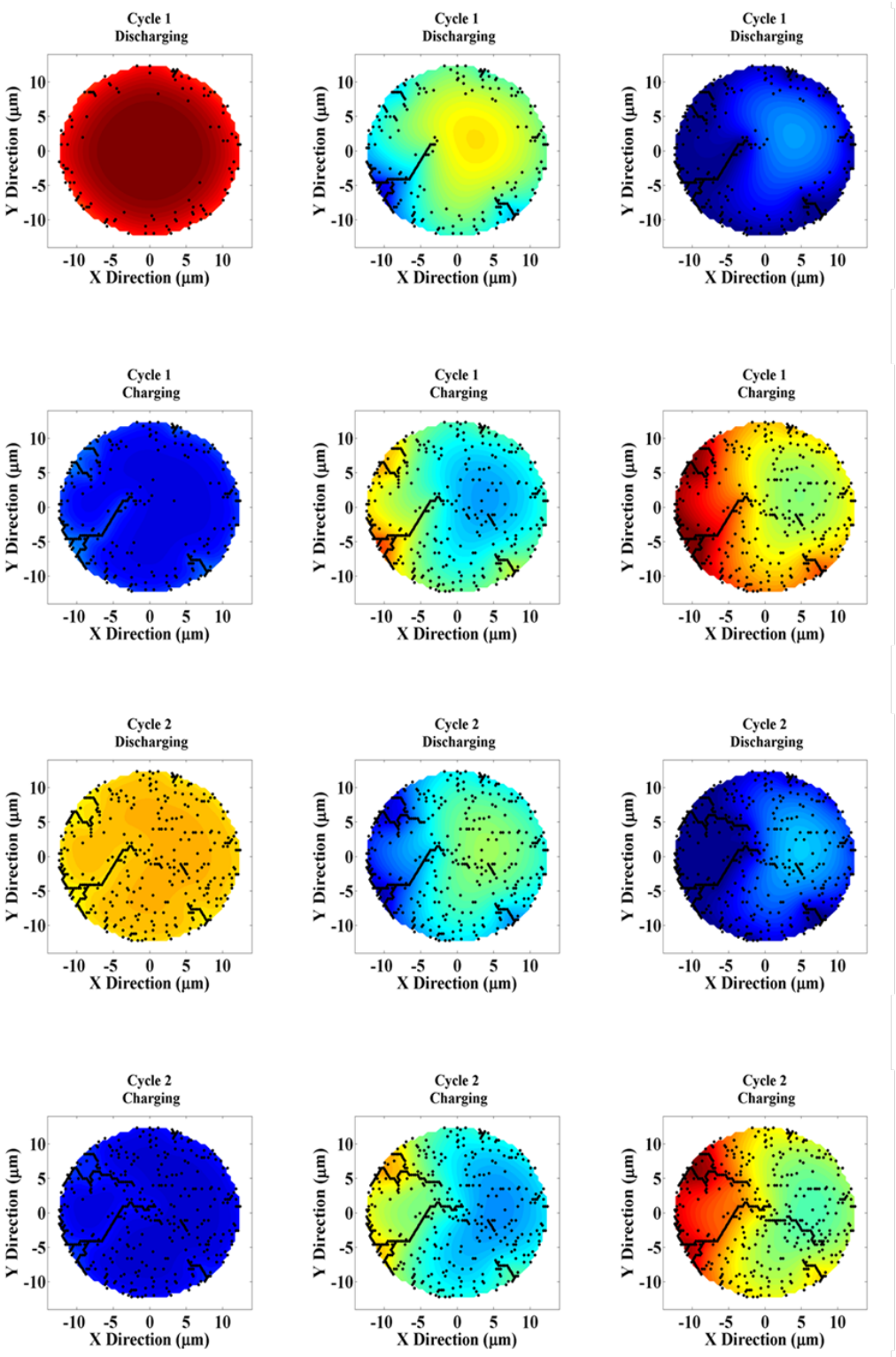

Figure 32: Concentration contour plots for cycling simulations

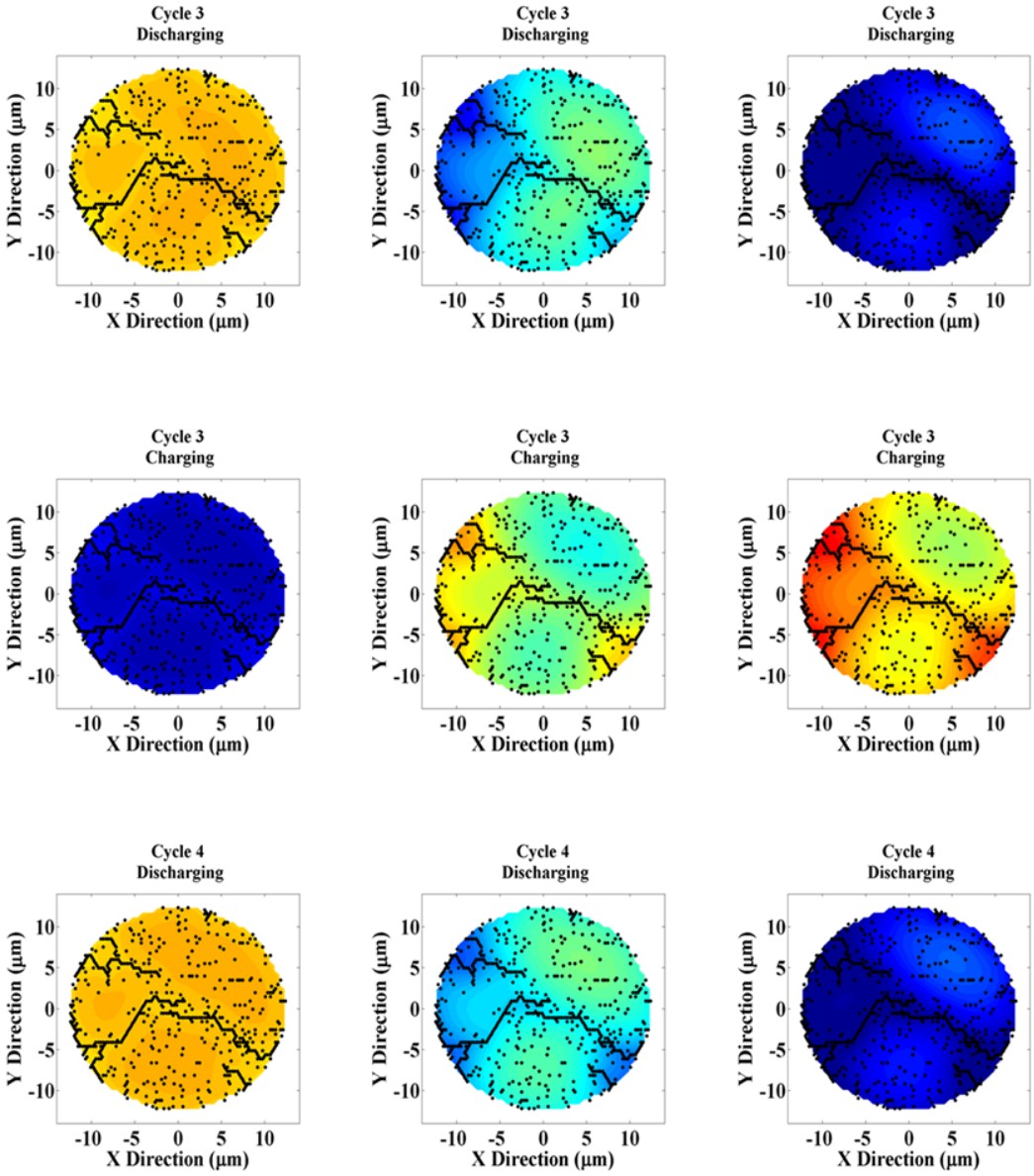

Figure 33: Concentration contour plots for cycling simulations (cont.)

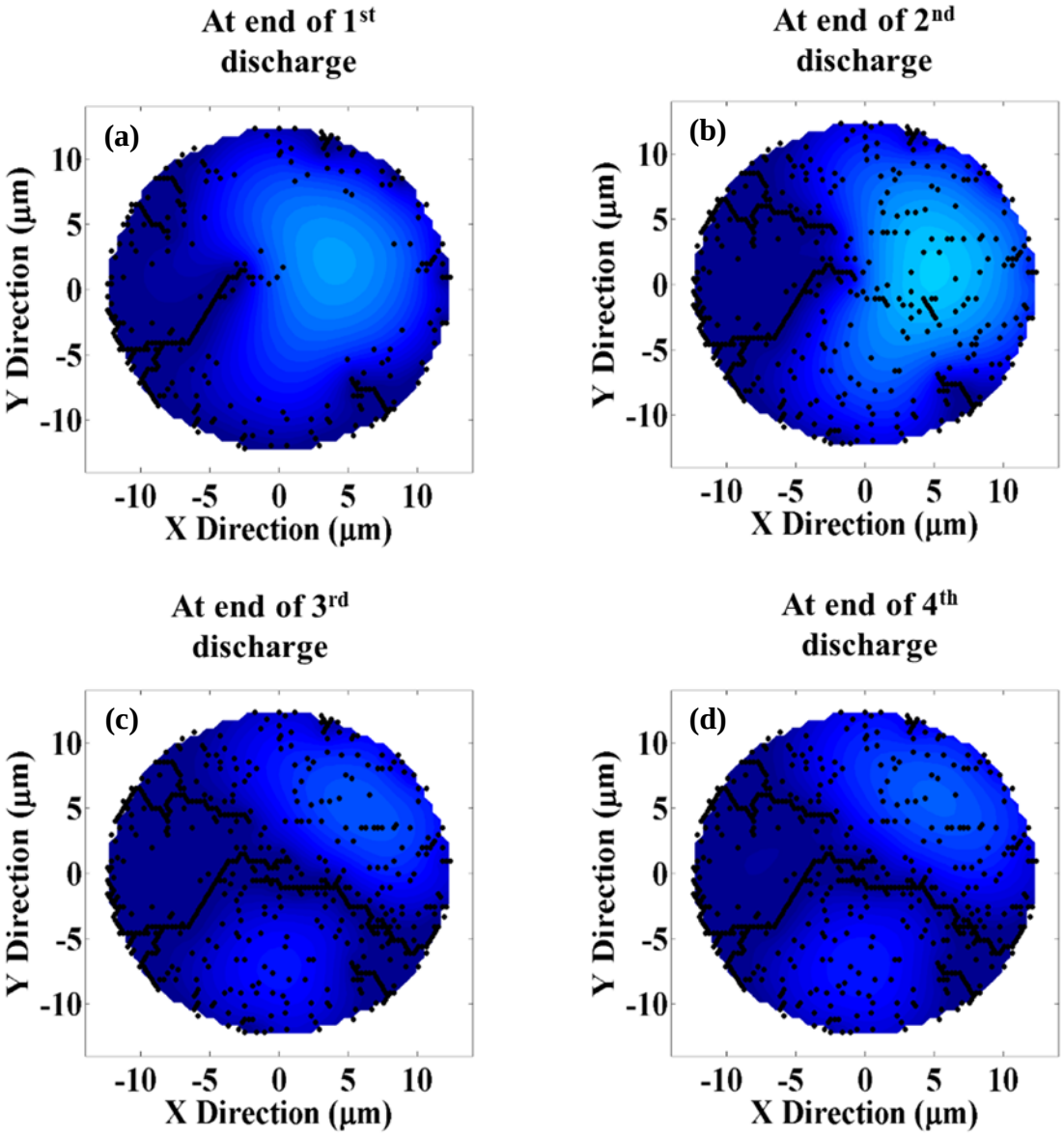

Figure 34: Concentration contour plots with microcracks superimposed (a) end of 1st discharge (b) end of 2nd discharge (c) end of 3rd discharge (d) end of 4th discharge

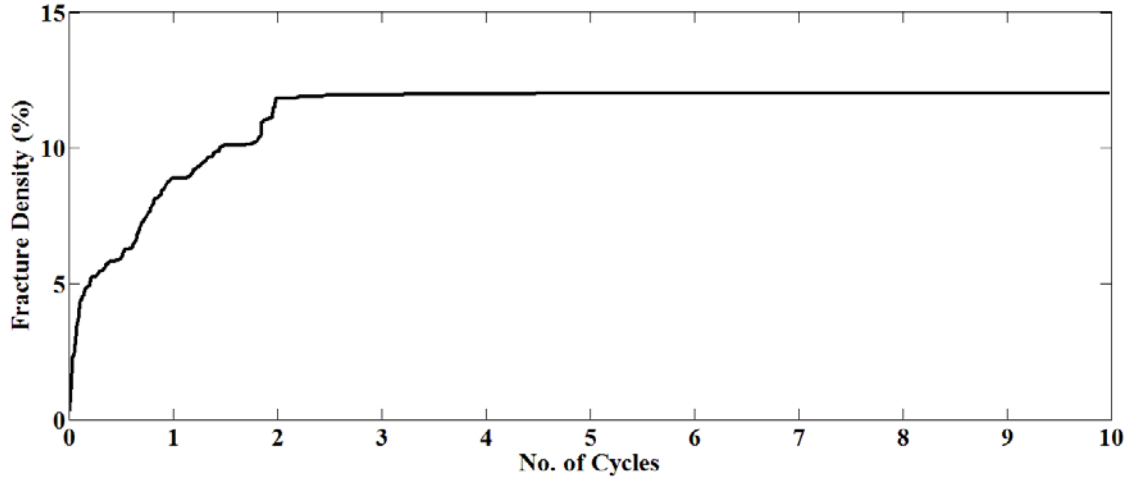

Figure 35: Cycling behavior - fracture density

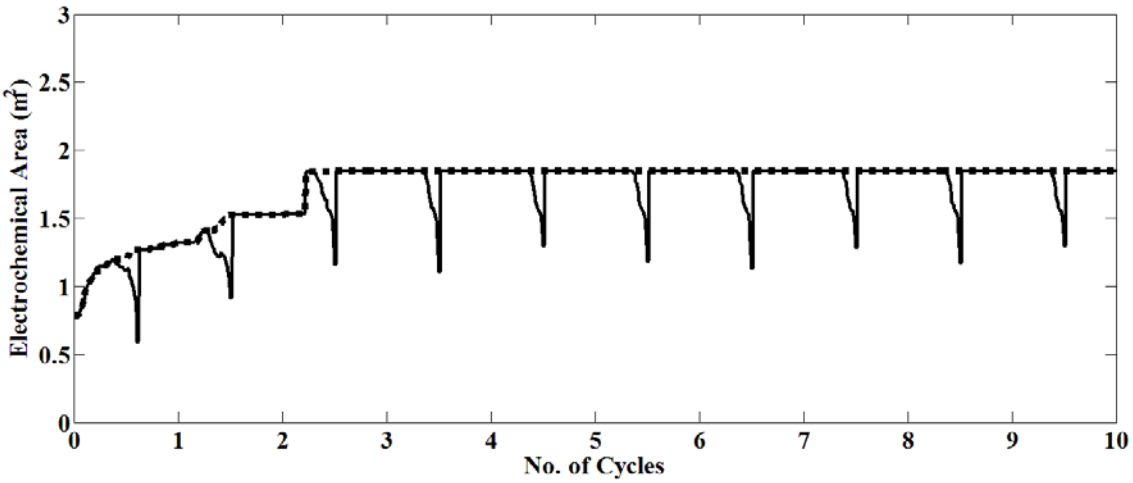

Figure 36: Cycling behavior - electrochemical area

The variation of bulk and surface concentration, normalized with the maximum lithium concentration, for the particle is plotted versus number of cycles in the fig. 36. It is logical that during the discharge half cycle, the surface concentration is lower than the

bulk concentration for the particle. During charge half cycle, the bulk concentration is lower than the surface concentration as lithium generating reactions take place at the surface of the particle. It is also evident from the figure that the concentration variation over each cycle gets more uniform with number of cycles. Hence, the difference between the maximum bulk concentrations reached at the end of two consecutive charge cycles decreases with number of cycles.

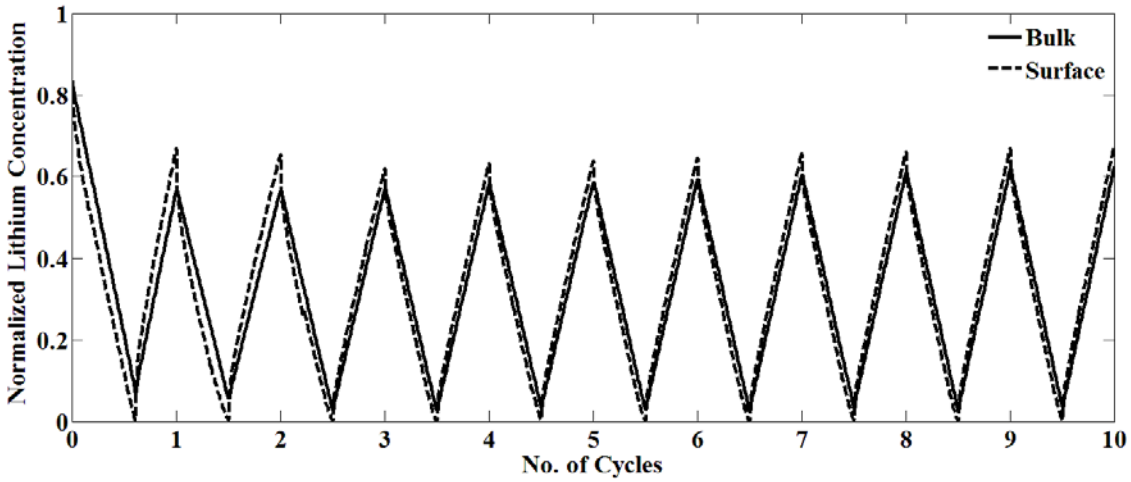

Figure 37: Cycling behavior – normalized concentration

Figure 37 displays the performance curves for the cell undergoing multiple charge-discharge cycles. The resulting voltage also follows a cyclic behavior. However, it is difficult to comment on the capacity of the cell over multiple charge-discharge cycles using this plot. Hence, in fig. 38, the cell voltage is plotted against the normalized time. Normalized time here means time divided by the theoretical time required for a

charge/discharge half cycle (for example, at 1C this would mean dividing time by 3600 seconds).

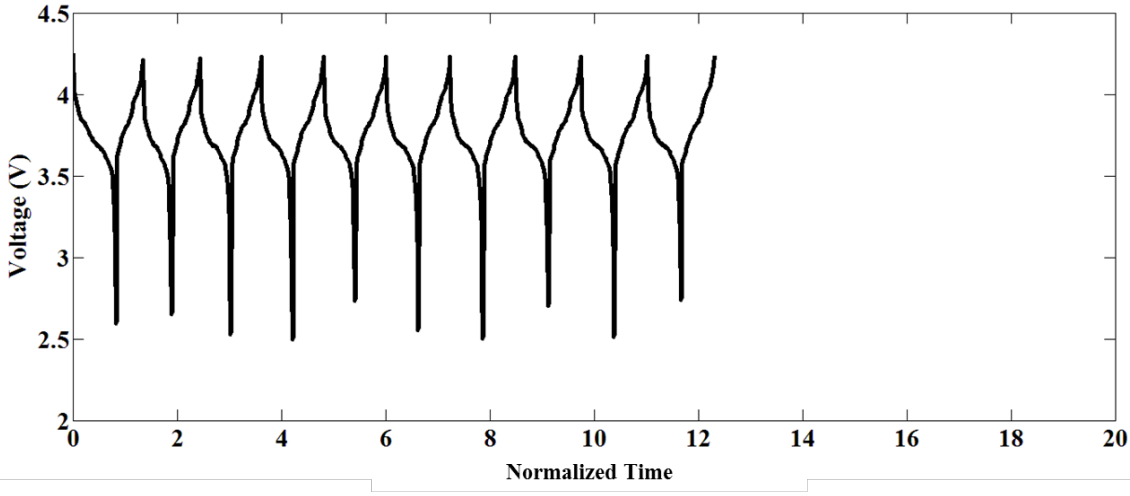

Figure 38: Cycling behavior – performance

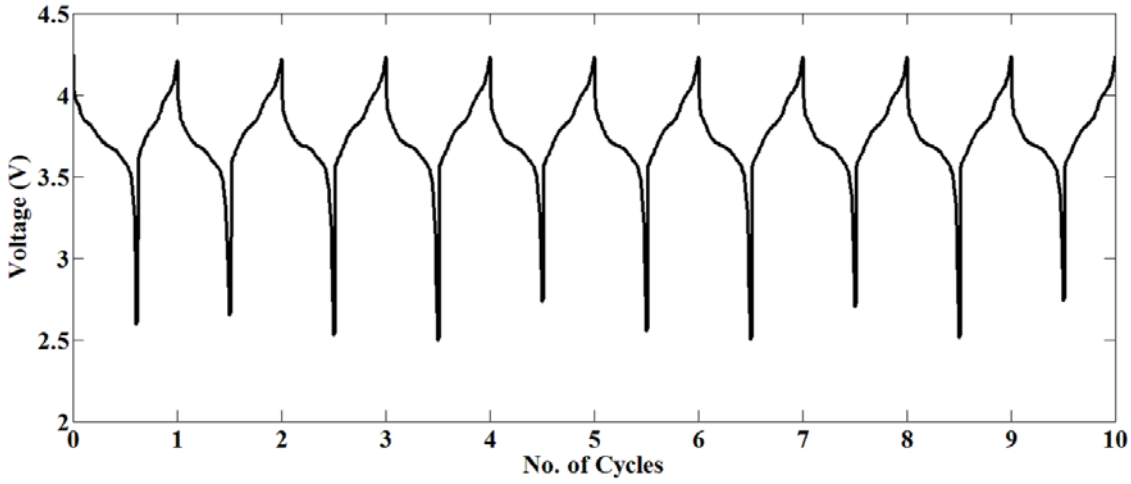

Figure 39: Cycling behavior – cycle wise performance

From figure 37, it is clear that the energy extracted or the capacity obtained from the particle, that is proportional to the area under the curve for the discharge process, is very low compared to the theoretical values. Up to some extent, this loss can be attributed to the charging protocol simulated. Constant current charging protocol cannot completely charge the active particles. Hence, the energy input to the cell during the charging process is also much lower than the theoretical value. Fig. 39 compares the discharge performance curves for the 1st and the 10th cycles. The capacity obtained in the 10th cycle is significantly lower than that in the 1st cycle. This highlights the capacity fade associated with cycling.

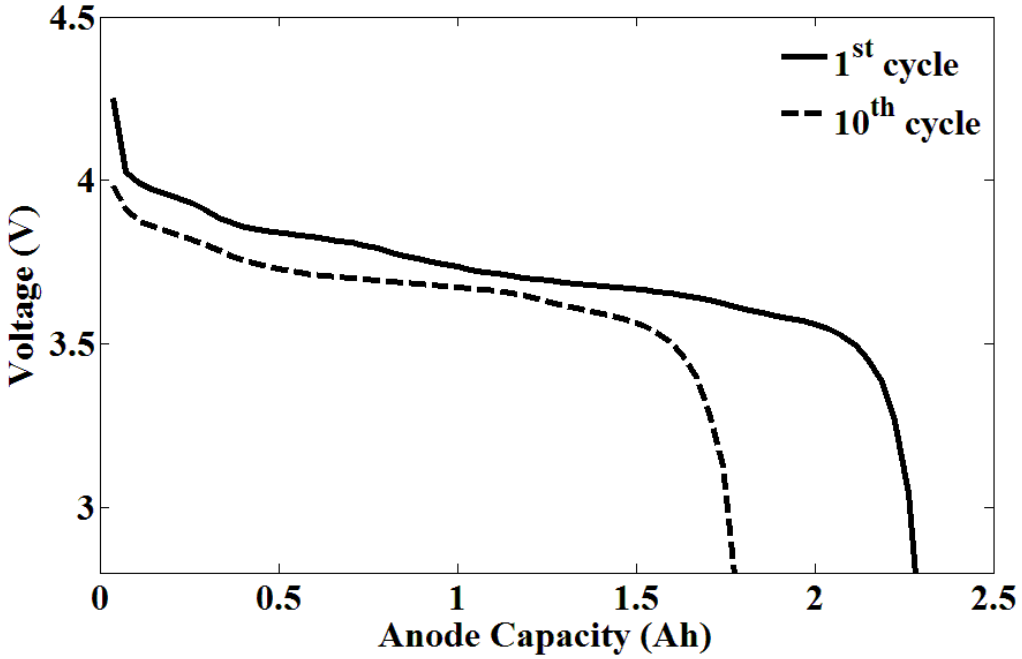

Figure 40: Cycling behavior – capacity fade

Next, in this chapter, the effect of various physicochemical factors on the mechanical degradation and performance of the cell over multiple cycles is analyzed.

Effect of rate of operation

Rate of operation is one of the most important physicochemical factor that drastically affects both, mechanical degradation and cell performance. Three different C-rates (C/2, 1C and 2C) are considered for this study. All the other physicochemical factors are kept constant (R = 12.5μm, 25°C) for the simulations. Figure 40 exhibits the evolution of fracture density with normalized time for the 3 C-rates mentioned above. Similar to the single discharge results, increasing the C-rate leads to an increase in the microcrack formation. The concentration contours at the end of 10th discharge cycle for the three cases are plotted in fig.41. The particle undergoing cycling at 2C has significantly greater microcrack formation compared to the particle operating at C/2 current. This implies that the electrode undergoing cycling at 2C current will have a higher growth in electrochemical area compared to the electrode operating at C/2 current (see fig. 42). Also, as observed in the single discharge case, at higher C-rates, the difference between actual and theoretical cycle time is higher. Thus, for the three cases considered, the 2C case completes 10 cycles in the least normalized time.

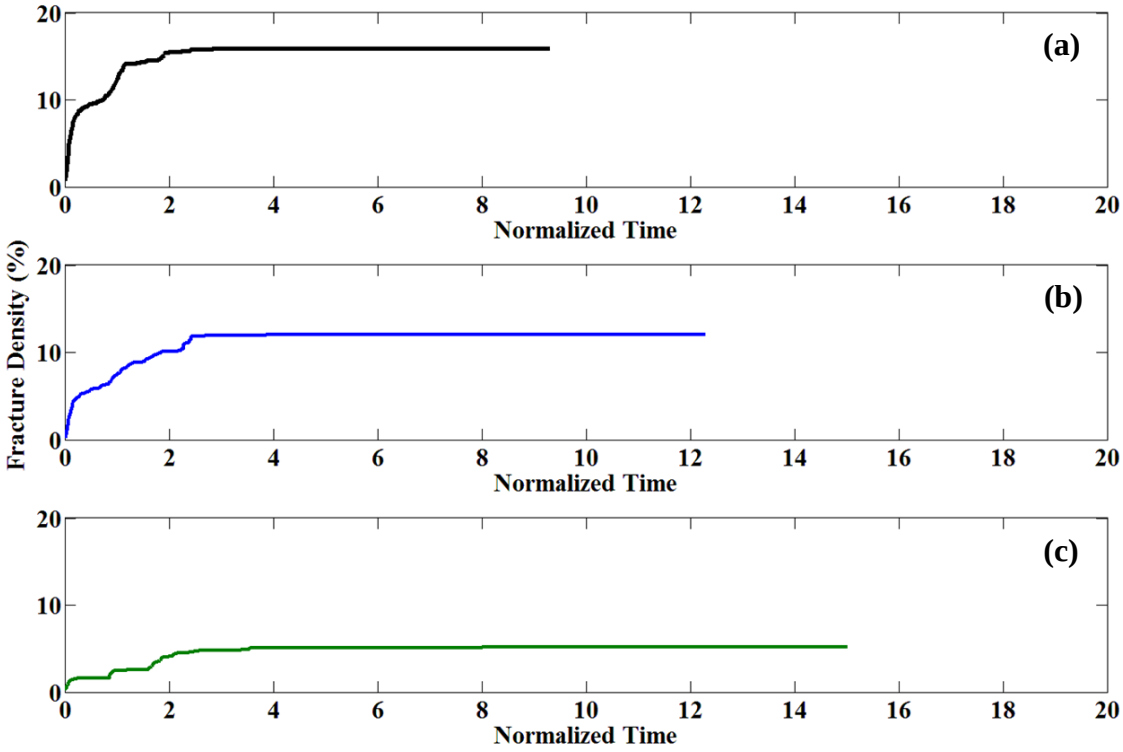

Figure 41: Effect of rate of operation – fracture density
(a) 2C (b) 1C (c) C/2

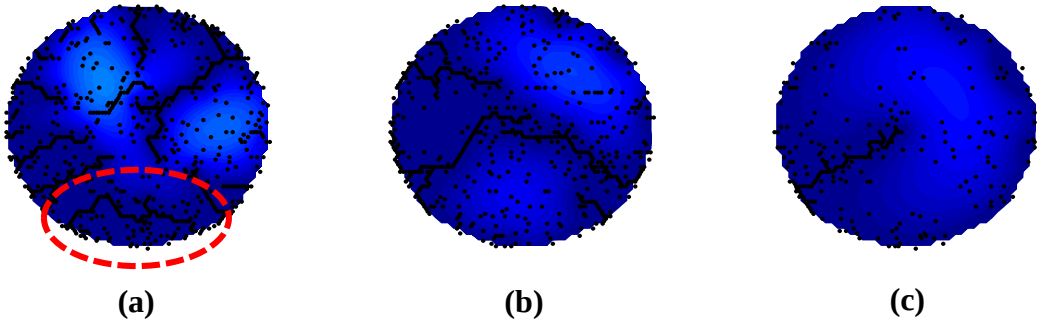

Figure 42: Concentration contour plots at the end of 10th discharge cycle
(a) 2C (b) 1C (c) C/2

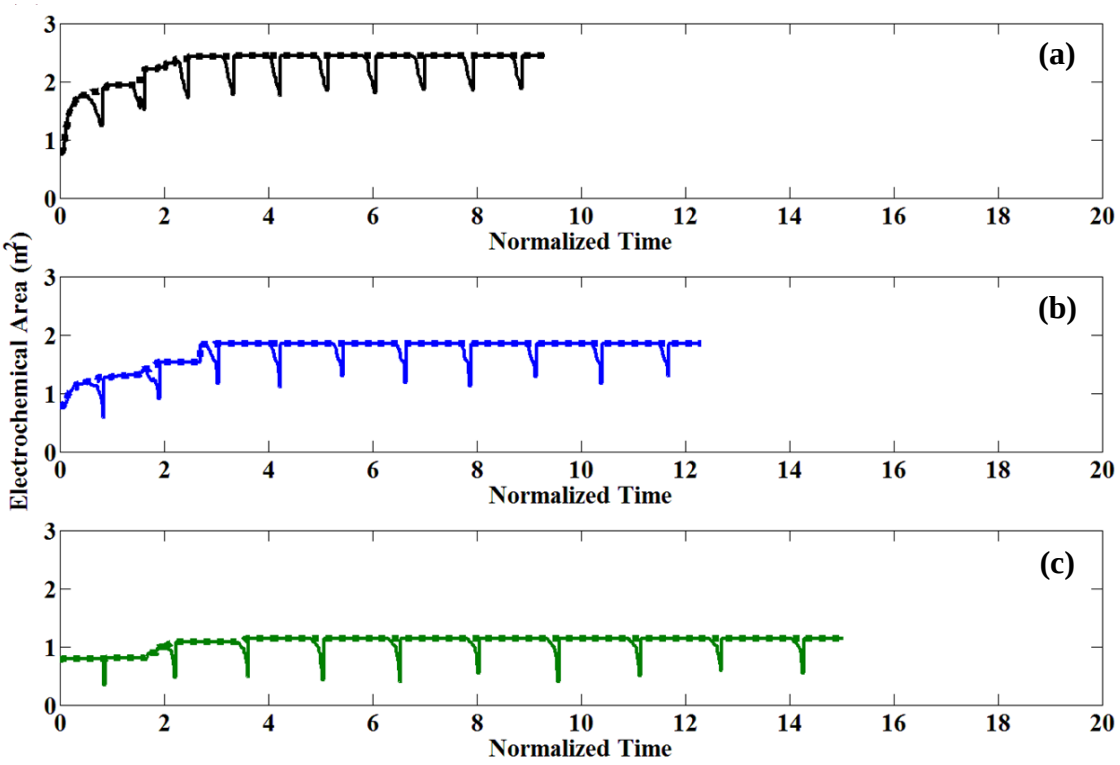

Figure 43: Effect of rate of operation – electrochemical area
(a) 2C (b) 1C (c) C/2

At higher C-rates, the rate of electrochemical reactions taking place at the electrochemically active surface area of the active particles is higher. Thus, the rate at which lithium is generated/consumed is higher than the rate at which it can diffuse through the particle. This leads to development of considerable concentration gradient within the particle. Hence, during discharge half cycle, the lithium concentration in the particle is lowest at the surface of the particle whereas during charge half cycle, surface of the particle has the maximum lithium concentration within the particle. This is evident from the normalized bulk and surface concentration evolution shown in fig. 43. The charge-discharge cycles have voltage as the stopping criteria. As voltage is dependent only on the

surface concentration of the particles, the concentration gradient within the electrode operating at 2C restricts the cell from charging/discharging completely.

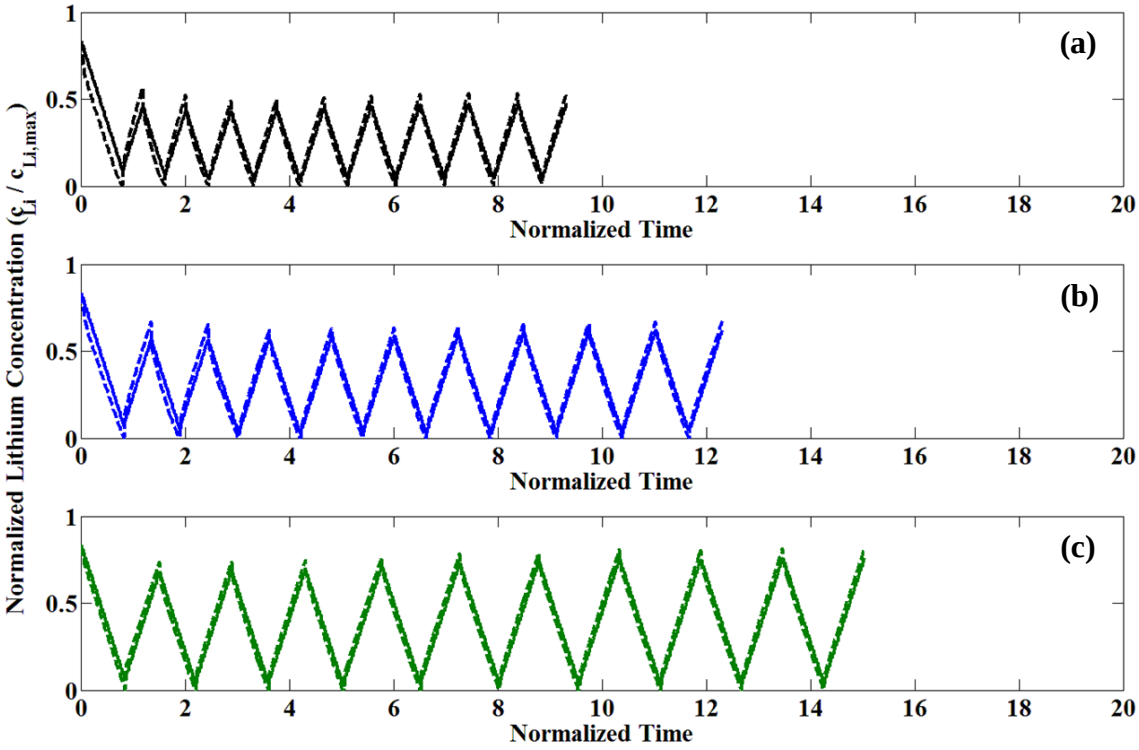

Figure 44: Effect of rate of operation – normalized concentration (a) 2C (b) 1C (c) C/2

Figure 44 compares the performance for the three C-rate operations. At the end of 10 cycles, the energy extracted from the cell operating at 2C current is minimum. This is evident from the distinctly smaller area under the voltage curve for the discharge cycles at 2C. However, lowering the C-rate results in an increase in the cell capacity.

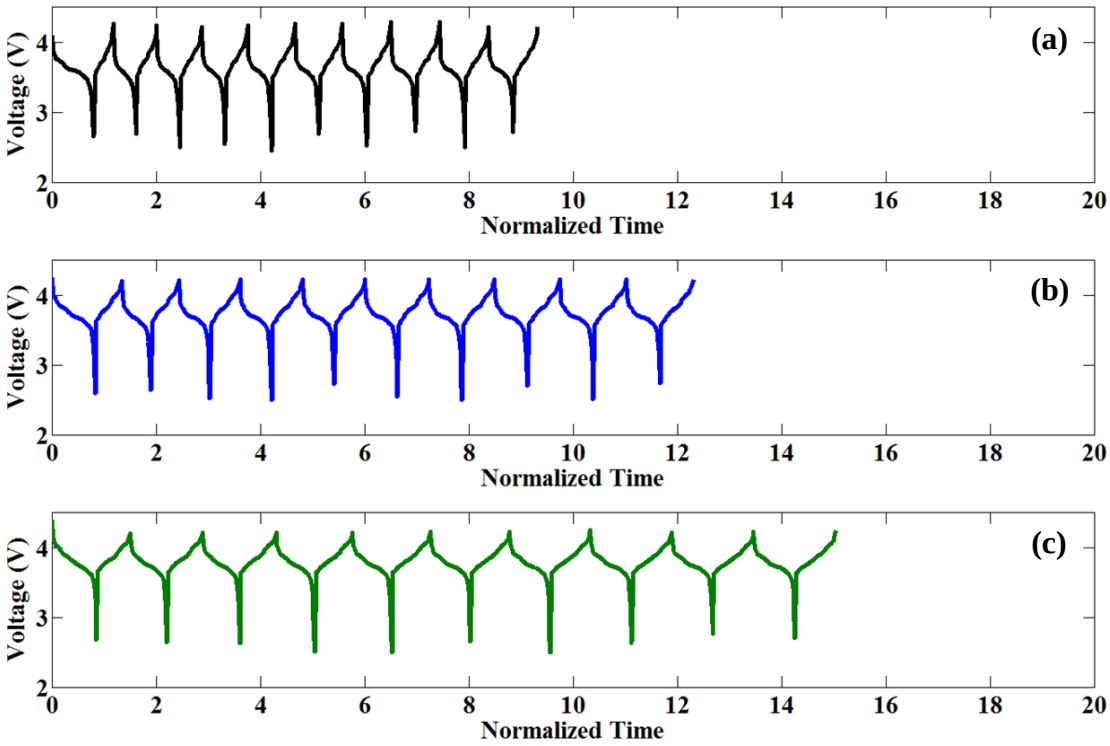

Figure 45: Effect of rate of operation – performance
(a) 2C (b) 1C (c) C/2

Fig. 45 has the cell voltage plotted against number of cycles for the three C-rates superimposed. Using this figure, the average voltage for each cycle can be easily compared for the three cases. The performance curve for the C/2 case completely envelopes the performance curve for 1C which itself envelopes the 2C performance curve. Thus, the average voltage for C/2 case is highest followed by the 1C case and then the 2C case. Hence, not only does lower C-rate give better cycling capacity, it also leads to higher average voltage.

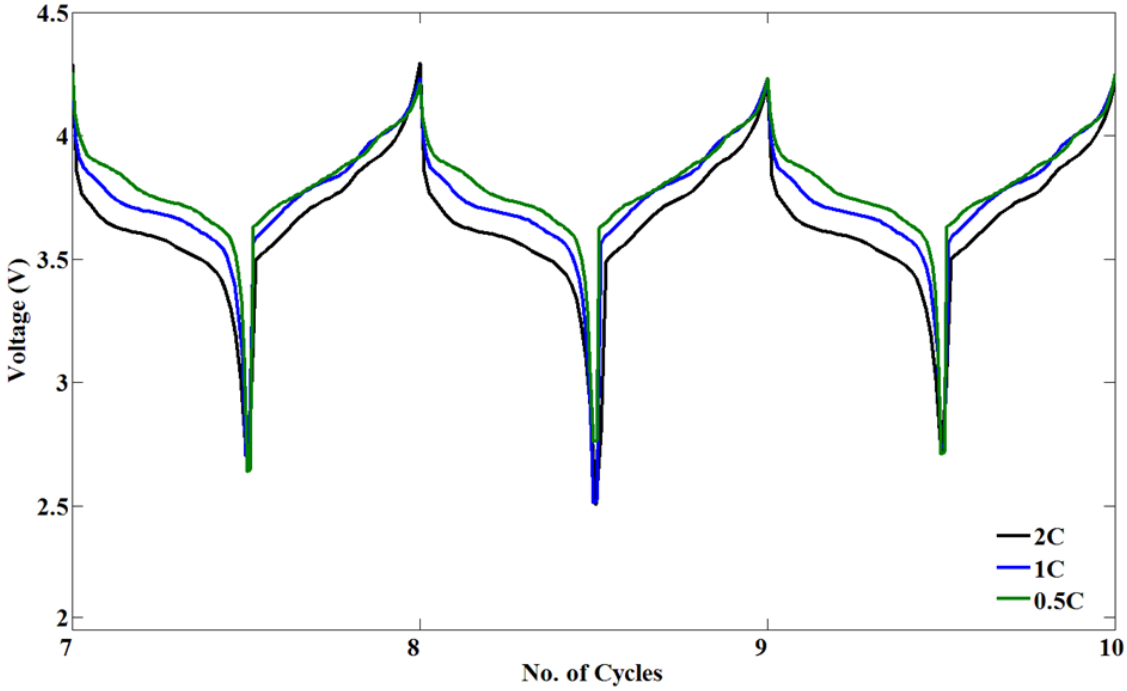

Figure 46: Cycling behavior – cycle wise performance

Effect of temperature

As discussed in chapter 3, temperature affects lithium transport within the active particle by changing the diffusivity. At lower temperatures, the diffusivity is very low implying poor transport of lithium. Temperature also affects the cell voltage by changing the open circuit potential of the electrodes. For investigating the effect of temperature on cell's cycling behavior, three temperatures (0°C, 25°C and 50°C) are considered. All the other physicochemical factors are kept constant (R = 12.5μm, 2C) for the simulations. Figure 46 shows the fracture evolution for the three cases. As observed in the single

discharge results, at lower temperatures the reduced diffusivity leads to development of large concentration gradient within the particle leading to greater mechanical degradation.

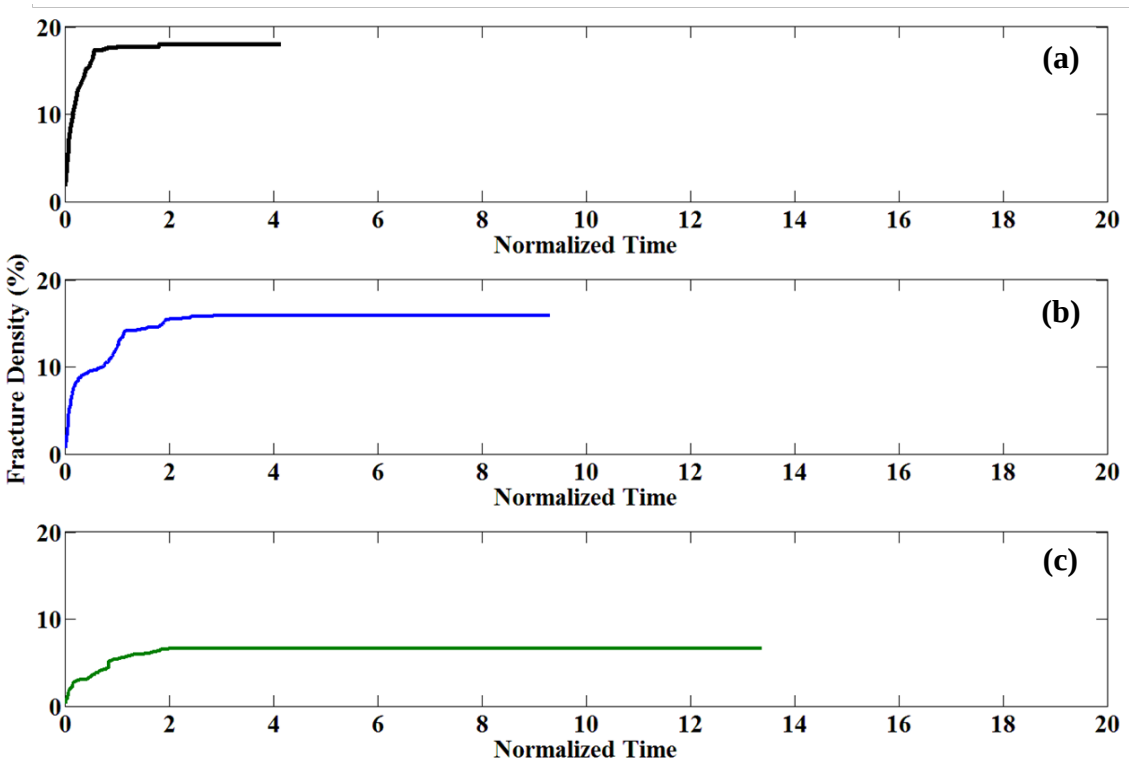

Figure 47:Effect of temperature – fracture density
(a) 0°C (b) 25°C (c) 50°C

Also, mechanical degradation and electrochemical area evolution both saturate after the initial few cycles. The increase in electrochemical area due to microcrack formation is maximum for the 0°C case and minimum for the 50°C case. Figure 47 exhibits the concentration contour plots with microcracks superimposed at the end of the 10th discharge cycle for the three cases. The particles operating at 0°C and 50°C exhibit extensive microcrack formation. Consequently, they also exhibit a large increase in the

electrochemically active surface area (see fig. 48). The presence of a relatively large concentration gradient can be observed for the 0°C case (fig. 47). Also, upon close scrutiny, particle disintegration due to coalescing of microcracks can be observed at 0°C and 25°C.

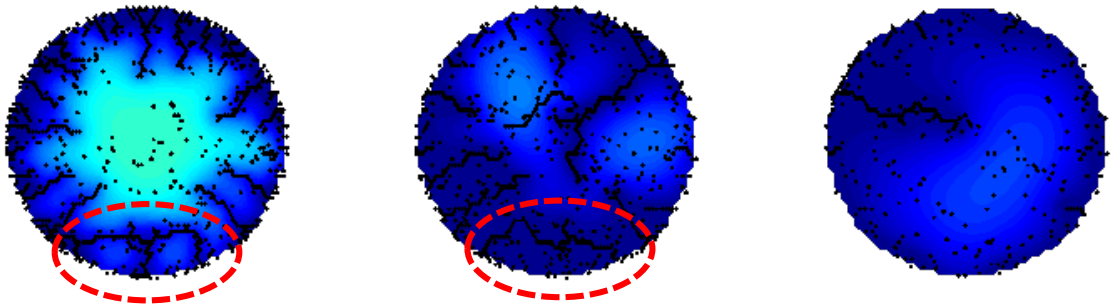

(a) **(b)** **(c)**

Figure 48: Concentration contour plots at the end of 10th discharge cycle (a) 0°C (b) 25°C (c) 50°C

The large concentration gradient existing between the electrochemical surface area and the core of the particle at 0°C implies that lithium from the active particle is not fully extracted. Similarly, at the end of constant current charge half cycle, the active particles are not full lithiated. At higher temperatures, improvement of lithium transport within the particle reduces the concentration gradient and thus charge/discharge processes lithiate/delihtiate the anode active particle better. This is reflected in the bulk concentration evolution shown in figure 49.

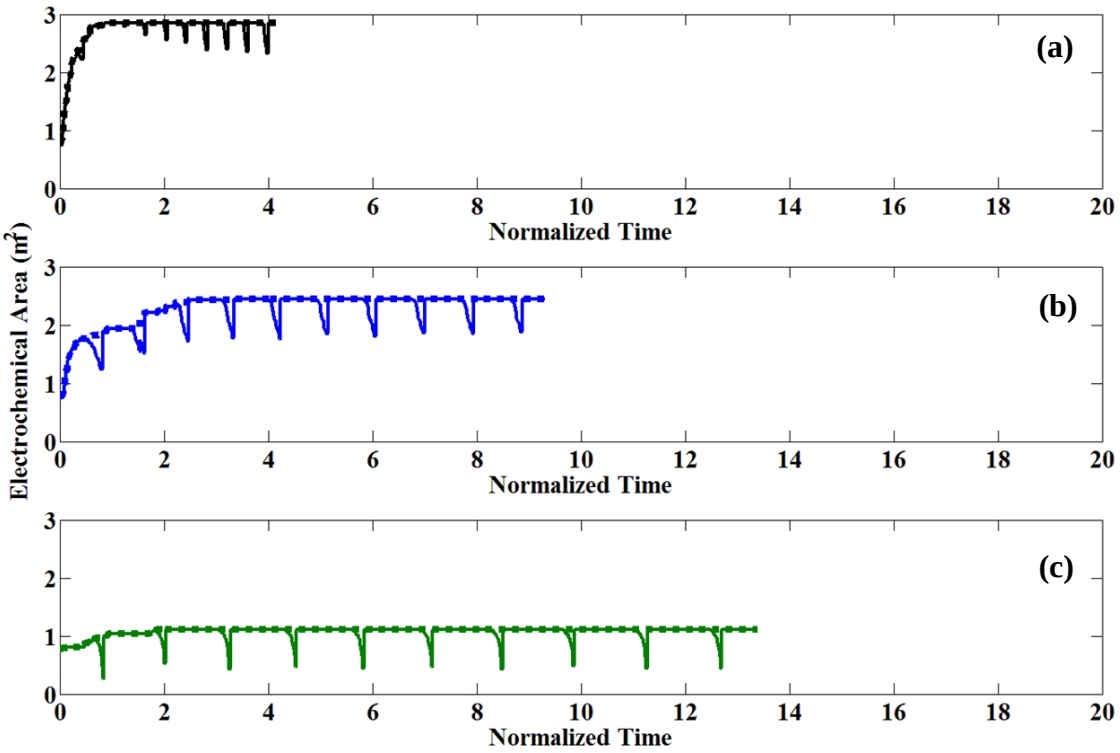

Figure 49: Effect of temperature – electrochemical area
(a) 0°C (b) 25°C (c) 50°C

As the charge/discharge processes do not fully lithiate/delithiate the anode active particles, a significantly lower cell capacity is observed for the 0°C case. As the temperature increases, improved cycling performance is observed (see fig.50). Also, superimposing the voltage vs. cycle plots for the three cases shows that the performance curve at 50°C envelopes the performance curve at 25°C which in turn envelopes the performance curve at 0°C. Thus, the average voltage at an operating temperature of 50°C is greater than that at 25°C which is greater than the average voltage at 0°C (see fig. 51).

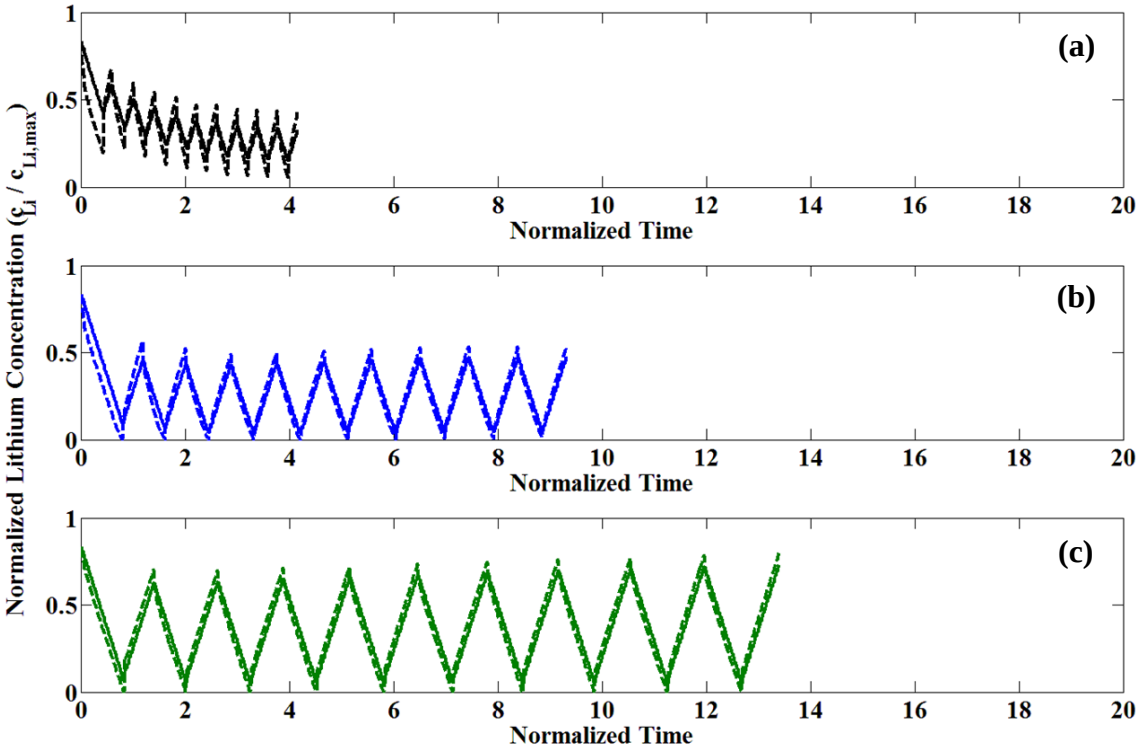

Figure 50: Effect of temperature – normalized concentration
(a) 0°C (b) 25°C (c) 50°C

As expected, cycling and single discharge behavior yield quite similar results. High rate of operation, low temperature and larger particle size lead to large concentration gradients within the particle. While this directly translates to poor performance for the above mentioned operating conditions, larger concentration gradient also implies more microcrack formation. The improvement in diffusion due to the formation of more number of electrochemically active microcracks tries to counter the poor diffusion and improve performance. However, as it can be seen from the results, the positive effect associated with increased mechanical degradation is unable to overcome the poor diffusion caused by the above mentioned operating conditions. It only reduces the magnitude of

performance drop that would have been otherwise been observed in a case where microcracks do not form (Single Particle model).

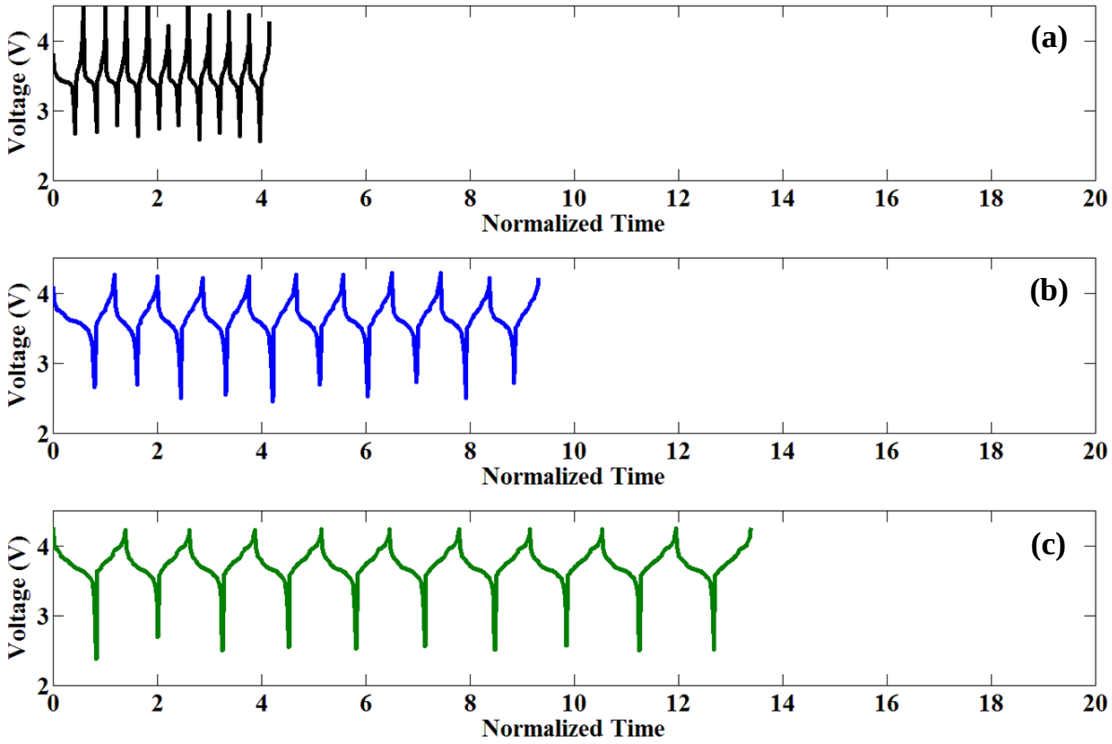

Figure 51: Effect of temperature – performance
(a) 0°C (b) 25°C (c) 50°C

Also, there exists a high possibility of particle disintegration at higher rate of operation, lower temperature and large particle size. This can prove to be undesirable as it can lead to particle isolation due to poor contact between the disintegrated active particle and the carbon additives.

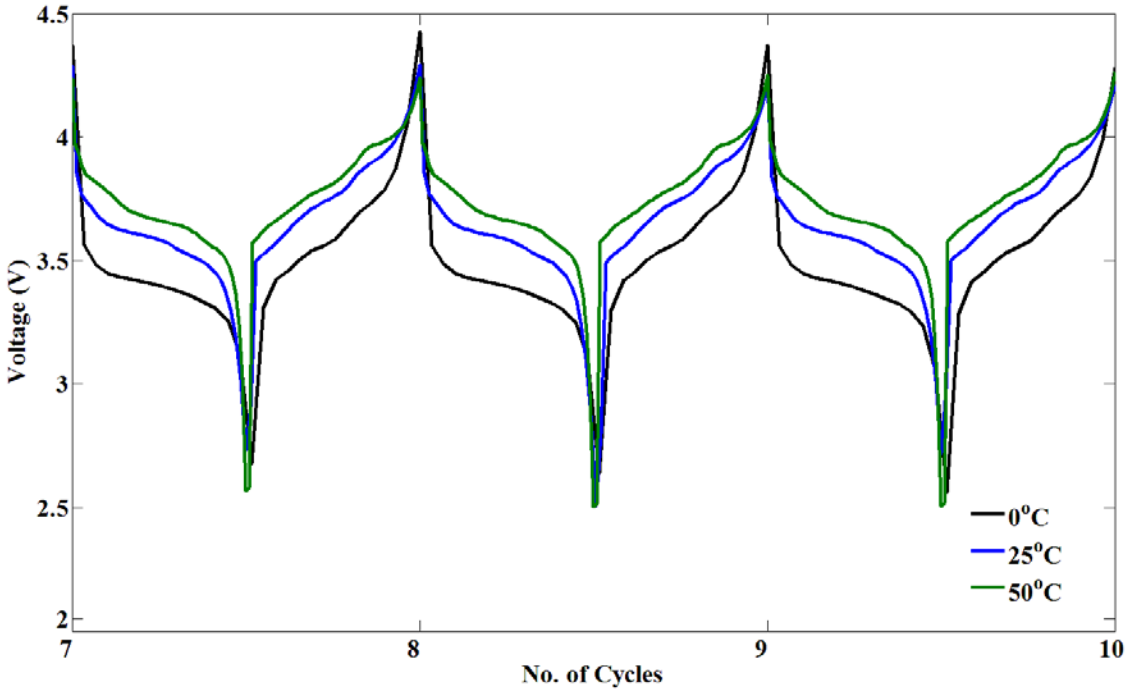

Figure 52: Effect of temperature – cycle wise performance

CHAPTER V

CONCLUSION AND FUTURE SCOPE

The mechano-electrochemical model developed in this study captures the intimate coupling between mechanical degradation and electrochemical behavior of the cell. Allowing for electrochemical reactions in the microcracks leads to preferential propagation of electrochemically active microcracks. Thus, microcracks are not uniformly distributed along the azimuthal direction of the particle. The microcrack patterns predicted by the model resemble the patterns observed in the SEM images of actual electrode active particles. Allowing for electrochemical reactions in the microcracks directly affects the lithium concentration distribution within the active particle. Like microcracks, lithium concentration within the active particle also varies in the azimuthal direction.

The performance predicted by the mechano-electrochemical model developed here is greater than that predicted by the single particle model. This is because the mechano-electrochemical model not only accounts for the lithium transport hindering effect of mechanical degradation but it also incorporates the lithium transport enhancing effect of mechanical degradation. That is, the electrochemically active microcracks increase the electrode surface area and reduce the effective diffusion length as they allow reactions to take place in the interior of the particle. The single particle model however, does not consider mechanics. Thus the diffusion length for the single particle model is equivalent to the radius of the particle and is thus fixed.

Mechano-electrochemical model for simulating the constant current cycling behavior is also developed. In certain cycling cases, disintegration of active particles due to coalescing of microcracks is also observed. This can lead to significant loss of cyclable lithium. The mechanical degradation in the active particles is found to be saturating by the end of first few cycles. The effect of physicochemical behavior on the mechanical degradation behavior of the electrode active particles has been investigated. It has been observed that higher operating temperature, lower operating current and smaller particle size lead to minimum mechanical degradation.

Experimentally, it is not possible to isolate the effect of mechanical degradation on the cell performance. In all the practical cases, mechanical degradation is often clubbed with chemical degradation (SEI formation). Mechanical degradation leads to microcrack formation and chemical degradation leads to formation of SEI layer on the electrochemically active microcrack surface. Over multiple cycles, this leads to a significant irreversible loss of lithium reducing the capacity of the cell considerably. Thus, further studies should look into the combined effect of SEI formation and microcrack propagation. This will prove crucial in investigating the capacity fade associated with cycling. Future studies can also study the cycling behavior of the electrodes using the constant current-constant voltage (CC-CV) charge protocol.

REFERENCES

1. Armand, M. and J.M. Tarascon, *Building better batteries.* Nature, 2008. **451**(7179): p. 652-657.
2. Hoel, M. and S. Kverndokk, *Depletion of fossil fuels and the impacts of global warming.* Resource and Energy Economics, 1996. **18**(2): p. 115-136.
3. Bruce, P.G., B. Scrosati, and J.M. Tarascon, *Nanomaterials for rechargeable lithium batteries.* Angewandte Chemie-International Edition, 2008. **47**(16): p. 2930-2946.
4. Hart, D., *Sustainable energy conversion: fuel cells - the competitive option?* Journal of Power Sources, 2000. **86**(1-2): p. 23-27.
5. Akella, A.K., R.P. Saini, and M.P. Sharma, *Social, economical and environmental impacts of renewable energy systems.* Renewable Energy, 2009. **34**(2): p. 390-396.
6. Turner, J.A., *A realizable renewable energy future.* Science, 1999. **285**(5428): p. 687-689.
7. Armaroli, N. and V. Balzani, *The future of energy supply: challenges and opportunities.* Angewandte Chemie-International Edition, 2007. **46**(1-2): p. 52-66.
8. Painuly, J.P., *Barriers to renewable energy penetration; a framework for analysis.* Renewable Energy, 2001. **24**(1): p. 73-89.
9. Cavallo, A.J., *Energy storage technologies for utility scale intermittent renewable energy systems.* Journal of Solar Energy Engineering-Transactions of the ASME, 2001. **123**(4): p. 387-389.

10. Ibrahim, H., A. Ilinca, and J. Perron, *Energy storage systems - characteristics and comparisons.* Renewable & Sustainable Energy Reviews, 2008. **12**(5): p. 1221-1250.

11. Beaudin, M., H. Zareipour, A. Schellenberglabe, and W. Rosehart, *Energy storage for mitigating the variability of renewable electricity sources: an updated review.* Energy for Sustainable Development, 2010. **14**(4): p. 302-314.

12. Barton, J.P. and D.G. Infield, *Energy storage and its use with intermittent renewable energy.* IEEE Transactions on Energy Conversion, 2004. **19**(2): p. 441-448.

13. Chen, H.S., et al., *Progress in electrical energy storage system- a critical review.* Progress in Natural Science, 2009. **19**(3): p. 291-312.

14. Dunn, B., H. Kamath, and J.M. Tarascon, *Electrical energy storage for the grid-a battery of choices.* Science, 2011. **334**(6058): p. 928-935.

15. Boulanger, A.G., A.C. Chu, S. Maxx, and D.L. Waltz, *Vehicle electrification-status and issues.* Proceedings of the IEEE, 2011. **99**(6): p. 1116-1138.

16. Valentine-Urbschat, M. and W. Bernhart, *Powertrain 2020–the future drives electric.* Roland Berger Strategy Consultants, 2009. **9**.

17. Lukic, S.M., J. Cao, R.C. Bansal, F. Rodriguez, and A. Emadi, *Energy storage systems for automotive applications.* Industrial electronics, IEEE Transactions on, 2008. **55**(6): p. 2258-2267.

18. Moura, S.J., J.B. Siegel, D.J. Siegel, H.K. Fathy, and A.G. Stefanopoulou. *Education on vehicle electrification: battery systems, fuel cells, and hydrogen*. in *Vehicle Power and Propulsion Conference (VPPC)*, 2010. IEEE.

19. Kasseris, E.P. and J.B. Heywood, *Comparative analysis of automotive powertrain choices for the next 25 years*. 2007, SAE Technical Paper.

20. Chiara, F. and M. Canova, *A review of energy consumption, management, and recovery in automotive systems, with considerations of future trends.* Proceedings of the Institution of Mechanical Engineers Part D-Journal of Automobile Engineering, 2013. **227**(6): p. 914-936.

21. Kalnaus, S., K. Rhodes, and C. Daniel, *A study of lithium ion intercalation induced fracture of silicon particles used as anode material in Li-ion battery.* Journal of Power Sources, 2011. **196**(19): p. 8116-8124.

22. Lukic, S.M., J. Cao, R.C. Bansal, F. Rodriguez, and A. Emadi, *Energy storage systems for automotive applications.* IEEE Transactions on Industrial Electronics, 2008. **55**(6): p. 2258-2267.

23. Ellis, B.L., K.T. Lee, and L.F. Nazar, *Positive electrode materials for Li-ion and Li-batteries.* Chemistry of Materials, 2010. **22**(3): p. 691-714.

24. Whittingham, M.S., *Lithium batteries and cathode materials.* Chemical Reviews, 2004. **104**(10): p. 4271-4301.

25. Guo, P., H. Song, and X. Chen, *Electrochemical performance of graphene nanosheets as anode material for lithium-ion batteries.* Electrochemistry Communications, 2009. **11**(6): p. 1320-1324.

26. Wu, Y.-P., E. Rahm, and R. Holze, *Carbon anode materials for lithium ion batteries.* Journal of Power Sources, 2003. **114**(2): p. 228-236.

27. Chen, J.J., *Recent progress in advanced materials for lithium ion batteries.* Materials, 2013. **6**(1): p. 156-183.

28. Megahed, S. and W. Ebner, *Lithium-ion battery for electronic applications.* Journal of Power Sources, 1995. **54**(1): p. 155-162.

29. Wagner, R., N. Preschitschek, S. Passerini, J. Leker, and M. Winter, *Current research trends and prospects among the various materials and designs used in lithium-based batteries.* Journal of Applied Electrochemistry, 2013. **43**(5): p. 481-496.

30. Fergus, J.W., *Recent developments in cathode materials for lithium ion batteries.* Journal of Power Sources, 2010. **195**(4): p. 939-954.

31. Rong, P. and M. Pedram, *An analytical model for predicting the remaining battery capacity of lithium-ion batteries.* Design, Automation and Test in Europe Conference and Exhibition, Proceedings, 2003: p. 1148-1149.

32. Tarascon, J.M. and M. Armand, *Issues and challenges facing rechargeable lithium batteries.* Nature, 2001. **414**(6861): p. 359-367.

33. Arora, P., R.E. White, and M. Doyle, *Capacity fade mechanisms and side reactions in lithium-ion batteries.* Journal of the Electrochemical Society, 1998. **145**(10): p. 3647-3667.

34. Cheng, Y.T. and M.W. Verbrugge, *Application of hasselman's crack propagation model to insertion electrodes.* Electrochemical and Solid State Letters, 2010. **13**(9): p. A128-A131.

35. Deshpande, R., Y.T. Cheng, M.W. Verbrugge, and A. Timmons, *Diffusion induced stresses and strain energy in a phase-transforming spherical electrode particle.* Journal of the Electrochemical Society, 2011. **158**(6): p. A718-A724.

36. Deshpande, R., M. Verbrugge, Y.T. Cheng, J. Wang, and P. Liu, *Battery cycle life prediction with coupled chemical degradation and fatigue mechanics.* Journal of the Electrochemical Society, 2012. **159**(10): p. A1730-A1738.

37. Renganathan, S., G. Sikha, S. Santhanagopalan, and R.E. White, *Theoretical analysis of stresses in a lithium ion cell.* Journal of the Electrochemical Society, 2010. **157**(2): p. A155-A163.

38. Zhang, X., W. Shyy, and A.M. Sastry, *Numerical simulation of intercalation-induced stress in Li-ion battery electrode particles (vol 154, pg A910, 2007).* Journal of the Electrochemical Society, 2007. **154**(12): p. S21-S21.

39. Chaboche, J.L.a.J.L., *Mechanics of solid materials.* Cambridge University Press, 1990.

40. Chen, C.F., P. Barai, and P.P. Mukherjee, *Diffusion induced damage and impedance response in lithium-ion battery electrodes.* Journal of the Electrochemical Society, 2014. **161**(14): p. A2138-A2152.

41. Christensen, J., *Modeling diffusion-induced stress in Li-ion cells with porous electrodes.* Journal of the Electrochemical Society, 2010. **157**(3): p. A366-A380.

42. Kerlau, M., J.A. Reimer, and E.J. Cairns, *Investigation of particle isolation in Li-ion battery electrodes using Li-7 NMR spectroscopy.* Electrochemistry Communications, 2005. **7**(12): p. 1249-1251.

43. Buqa, H., et al., *SEI film formation on highly crystalline graphitic materials in lithium-ion batteries.* Journal of Power Sources, 2006. **153**(2): p. 385-390.

44. Chen, C.F. and P.P. Mukherjee, *Probing the morphological influence on solid electrolyte interphase and impedance response in intercalation electrodes.* Physical Chemistry Chemical Physics, 2015. **17**(15): p. 9812-9827.

45. Huang, L.H., Z.H. Min, and Q.Y. Zhang, *Solid electrolyte inter-phase on graphite anodes in Li-ion batteries.* Reviews on Advanced Materials Science, 2014. **36**(1): p. 13-20.

46. Lee, H., et al., *SEI layer-forming additives for LiNi0.5Mn1.5O4/graphite 5 V Li-ion batteries.* Electrochemistry Communications, 2007. **9**(4): p. 801-806.

47. Ploehn, H.J., P. Ramadass, and R.E. White, *Solvent diffusion model for aging of lithium-ion battery cells.* Journal of the Electrochemical Society, 2004. **151**(3): p. A456-A462.

48. Rashid, M. and A. Gupta, *Mathematical model for combined effect of SEI formation and gas evolution in Li-ion batteries.* ECS Electrochemistry Letters, 2014. **3**(10): p. A95-A98.

49. Smith, A.J., J.C. Burns, X.M. Zhao, D.J. Xiong, and J.R. Dahn, *A high precision coulometry study of the SEI growth in Li/graphite cells.* Journal of the Electrochemical Society, 2011. **158**(5): p. A447-A452.

50. Barre, A., et al., *A review on lithium-ion battery ageing mechanisms and estimations for automotive applications.* Journal of Power Sources, 2013. **241**: p. 680-689.

51. Christensen, J. and J. Newman, *Stress generation and fracture in lithium insertion materials.* Journal of Solid State Electrochemistry, 2006. **10**(5): p. 293-319.

52. Christensen, J. and J. Newman, *A mathematical model of stress generation and fracture in lithium manganese oxide.* Journal of the Electrochemical Society, 2006. **153**(6): p. A1019-A1030.

53. Wang, H.F., Y.I. Jang, B.Y. Huang, D.R. Sadoway, and Y.T. Chiang, *TEM study of electrochemical cycling-induced damage and disorder in LiCoO2 cathodes for rechargeable lithium batteries.* Journal of the Electrochemical Society, 1999. **146**(2): p. 473-480.

54. Harris, S.J., R.D. Deshpande, Y. Qi, I. Dutta, and Y.T. Cheng, *Mesopores inside electrode particles can change the Li-ion transport mechanism and diffusion-induced stress.* Journal of Materials Research, 2010. **25**(8): p. 1433-1440.

55. Qi, Y. and S.J. Harris, *In situ observation of strains during lithiation of a graphite electrode.* Journal of the Electrochemical Society, 2010. **157**(6): p. A741-A747.

56. Woodford, W.H., Y.M. Chiang, and W.C. Carter, *Electrochemical shock in ion-intercalation materials with limited solid-solubility.* Journal of the Electrochemical Society, 2013. **160**(8): p. A1286-A1292.

57. Grantab, R. and V.B. Shenoy, *Location and orientation-dependent progressive crack propagation in cylindrical graphite electrode particles.* Journal of the Electrochemical Society, 2011. **158**(8): p. A948-A954.

58. Cheng, Y.T. and M.W. Verbrugge, *Diffusion-induced stress, interfacial charge transfer, and criteria for avoiding crack initiation of electrode particles.* Journal of the Electrochemical Society, 2010. **157**(4): p. A508-A516.

59. Zhao, K.J., M. Pharr, J.J. Vlassak, and Z.G. Suo, *Fracture of electrodes in lithium-ion batteries caused by fast charging.* Journal of Applied Physics, 2010. **108**(7).

60. Barai, P. and P.P. Mukherjee, *Stochastic analysis of diffusion induced damage in lithium-ion battery electrodes.* Journal of the Electrochemical Society, 2013. **160**(6): p. A955-A967.

61. Xu, J.G., R.D. Deshpande, J. Pan, Y.T. Cheng, and V.S. Battaglia, *Electrode side reactions, capacity loss and mechanical degradation in lithium-ion batteries.* Journal of the Electrochemical Society, 2015. **162**(10): p. A2026-A2035.

62. An, K., P. Barai, K. Smith, and P.P. Mukherjee, *Probing the thermal implications in mechanical degradation of lithium-ion battery electrodes.* Journal of the Electrochemical Society, 2014. **161**(6): p. A1058-A1070.

63. Gomadam, P.M., J.W. Weidner, R.A. Dougal, and R.E. White, *Mathematical modeling of lithium-ion and nickel battery systems.* Journal of Power Sources, 2002. **110**(2): p. 267-284.

64. Guo, M., G. Sikha, and R.E. White, *Single-particle model for a lithium-ion cell: thermal behavior.* Journal of the Electrochemical Society, 2011. **158**(2): p. A122-A132.

65. Santhanagopalan, S., Q.Z. Guo, P. Ramadass, and R.E. White, *Review of models for predicting the cycling performance of lithium ion batteries.* Journal of Power Sources, 2006. **156**(2): p. 620-628.

66. Song, L. and J.W. Evans, *Electrochemical-thermal model of lithium polymer batteries.* Journal of the Electrochemical Society, 2000. **147**(6): p. 2086-2095.

67. Doyle, M., J. Newman, A.S. Gozdz, C.N. Schmutz, and J.M. Tarascon, *Comparison of modeling predictions with experimental data from plastic lithium ion cells.* Journal of the Electrochemical Society, 1996. **143**(6): p. 1890-1903.

68. Nukala, P.K.V.V., S. Zapperi, and S. Simunovic, *Statistical properties of fracture in a random spring model.* Physical Review E, 2005. **71**(6).

69. Zhao, G.F., J.N. Fang, and J. Zhao, *A 3D distinct lattice spring model for elasticity and dynamic failure.* International Journal for Numerical and Analytical Methods in Geomechanics, 2011. **35**(8): p. 859-885.

70. Barai, P., K. Smith, C.F. Chen, G.H. Kim, and P.P. Mukherjee, *Reduced order modeling of mechanical degradation induced performance decay in lithium-ion battery porous electrodes.* Journal of the Electrochemical Society, 2015. **162**(9): p. A1751-A1771.

71. Matasso, A., D. Wong, D. Wetz, and F. Liu, *Effects of high-rate cycling on the bulk internal pressure rise and capacity degradation of commercial LiCoO2 cells.* Journal of the Electrochemical Society, 2015. **162**(6): p. A885-A891.

72. Narayanrao, R., M.M. Joglekar, and S. Inguva, *A phenomenological degradation model for cyclic aging of lithium ion cell materials.* Journal of the Electrochemical Society, 2013. **160**(1): p. A125-A137.

73. Smith, A.J., H.M. Dahn, J.C. Burns, and J.R. Dahn, *Long-term low-rate cycling of LiCoO2/graphite Li-ion cells at 55 degrees C.* Journal of the Electrochemical Society, 2012. **159**(6): p. A705-A710.

74. Takahashi, K., et al., *Mechanical degradation of graphite/PVDF composite electrodes: A model-experimental study.* Journal of The Electrochemical Society, 2016. **163**(3): p. A385-A395.

75. Takahashi, K. and V. Srinivasan, *Examination of graphite particle cracking as a failure mode in lithium-ion batteries: A model-experimental study.* Journal of the Electrochemical Society, 2015. **162**(4): p. A635-A645.